Title Page

Selective Inhibition of Autotaxin is Efficacious in Mouse Models of Liver Fibrosis

Gretchen Bain, Kristen E. Shannon, Fei Huang , Janice Darlington, Lance Goulet, Patricia Prodanovich, Gina L. Ma, Angelina M. Santini, Adam J. Stein, Dave Lonergan, Christopher D. King, Imelda Calderon, Andiliy Lai, John H. Hutchinson and Jilly F. Evans

PharmAkea Inc, San Diego, California: GB, KES, FH, JD, LG, PP, GLM, AMS, DL, CDK, IC, AL, JHH and JEF

Cayman Chemical Company, Ann Arbor, Michigan: AJS

Running Title Page

Autotaxin Inhibition Attenuates Mouse Liver Fibrosis

Corresponding Author:

Gretchen Bain

3030 Bunker Hill Street, Suite 300

San Diego, CA 92109

Ph: 858-764-3872

gbain@pharmakea.com

Number of text pages: 28

Number of Tables: 3

Number of Figures: 7

Number of References: 45

Number of words in Abstract: 194

Number of words in Introduction: 754

Number of words in Discussion: 1693

Abbreviations:

4-AAP - 4-aminoantipyrine

ALT – alanine transaminase

ALP – alkaline phosphatase

AST – aspartate transaminase

ATX – autotaxin

BALF - bronchoalveolar lavage fluid

BID – twice daily

CCl_4 – carbon tetrachloride

CDAHFD – choline-deficient, amino acid-defined, high-fat diet

DMSO - dimethylsulfoxide

ENPP – ectonucleotide pyrophosphatase phosphodiesterase

GLPG1690 - 2-((2-ethyl-6-(4-(2-(3-hydroxyazetidin-1-yl)-2-oxoethyl)piperazin-1-yl)-8-methylimidazo[1,2-a]pyridin-3-yl)(methyl)amino)-4-(4-fluorophenyl)thiazole-5-carbonitrile

GPCR – G protein-coupled receptor

H&E – hematoxylin and eosin

HA – hyaluronic acid

HCC – hepatocellular carcinoma

HRP – horse-radish peroxidase

IPF – idiopathic pulmonary fibrosis

i.v. - intravenous

LPA – lysophosphatidic acid

LPC – lysophosphatidylcholine

LysoPLD – lysophospholipase D

NAFLD – Non-alcoholic fatty liver disease

NAS – NAFLD activity score

NASH – Non-alcoholic steatohepatitis

NC – normal chow

nm - nanometer

MC – methylcellulose

QD – once daily

PAT-048 - 3-[6-chloro-7-fluoro-2-methyl-1-(1-propyl)-1*H*-pyrazol-4-yl-1*H*-indol-3-ylsulfanyl]-2-fluoro-benzoic sodium salt

PAT-505 – [3-((6-chloro-2-cyclopropyl-1-(1-ethyl-1H-pyrazol-4-yl)-7-fluoro-1H-indol-3-yl) thio)-2-fluorobenzoic acid sodium salt]

PD - pharmacodynamic

PF-8380 - 3,5-dichlorobenzyl 4-(3-oxo-3-(2-oxo-2,3-dihydrobenzo[d]oxazol-6-yl)propyl)piperazine-1-carboxylate

PK - pharmacokinetic

pNP-TMP - thymidine 5’-monophosphate p-nitrophenyl ester

PMSF – phenylmethylsulfonyl fluoride

p.o. - oral

PSR – picrosirius red

SMA – smooth muscle actin

Tg - triglycerides

TOOS - N-ethyl-N-(2-hydroxy-3-sulfopropyl)-m-toluidine

Recommended section assignment: Drug Discovery and Translational Medicine

Abstract

Autotaxin (ATX) is a secreted glycoprotein that converts lysophosphatidylcholine (LPC) to the bioactive phospholipid lysophosphatidic acid (LPA) and is the major enzyme generating circulating LPA. Inhibition of LPA signaling has profound anti-fibrotic effects in multiple organ systems including the lung, kidney, skin and peritoneum. However, other LPA-generating pathways exist and the role of ATX in localized tissue LPA production and fibrosis remains unclear and controversial. In this study, we describe the preclinical pharmacological, pharmacokinetic and pharmacodynamic properties of a novel small-molecule ATX inhibitor [3-((6-chloro-2-cyclopropyl-1-(1-ethyl-1H-pyrazol-4-yl)-7-fluoro-1H-indol-3-yl) thio)-2-fluorobenzoic acid sodium salt] (PAT-505). PAT-505 is a potent, selective, non-competitive inhibitor that displays significant inhibition of ATX activity in plasma and liver tissue after oral administration. When dosed therapeutically in a STAM™ model of non-alcoholic steatohepatitis (NASH), PAT-505 treatment resulted in a small, but significant, improvement in fibrosis with only minor improvements in hepatocellular ballooning and hepatic inflammation. In a choline-deficient high-fat diet model of NASH, therapeutic treatment with PAT-505 robustly reduced liver fibrosis with no significant effect on steatosis, hepatocellular ballooning and inflammation. These data demonstrate that inhibiting autotaxin is anti-fibrotic and may represent a novel therapeutic approach for the treatment of multiple fibrotic liver diseases, including NASH.

Introduction

Autotaxin is a secreted glycoprotein that was initially characterized as an autocrine motility stimulating factor for melanoma cells and was later shown to be the only member of the ectonucleotide pyrophosphatase/phosphodiesterase (ENPP) family that has lysophospholipase D (lysoPLD) activity (Stracke et al., 1992; Umezu-Goto et al., 2002). Mice heterozygous for an autotaxin deletion have approximately 50% circulating LPA compared to wild-type controls (Tanaka et al., 2006; van Meeteren et al., 2006) and ATX-depleted human serum displays negligible lysoPLD activity (Nakamura et al., 2007), thus validating autotaxin as the major enzyme producing circulating LPA. LPA signals through a family of at least six GPCRs designated LPA1-LPA6 to regulate diverse cellular processes including proliferation, contraction, migration, differentiation and survival. As a result, LPA is involved in a number of physiological and pathophysiological processes including angiogenesis, neurogenesis, hair follicle development, cancer progression/metastasis and fibrogenesis (Aikawa et al., 2015).

LPA-LPA1 signaling has been shown to contribute to the pathogenesis of fibrosis in multiple organs including the lung, kidney, skin and peritoneum (Pradere et al., 2007; Pradere et al., 2008; Tager et al., 2008; Swaney et al., 2010; Castelino et al., 2011; Swaney et al., 2011; Sakai et al., 2013) and an LPA1-selective antagonist is currently in a Phase II idiopathic pulmonary fibrosis (IPF) study (NCT01766817). However, activation of LPA2 also promotes bleomycin-induced lung injury and fibrosis (Geng et al., 2012; Huang et al., 2013). Therefore, ATX inhibition may show improved efficacy in attenuating fibrosis compared to LPA1-selective antagonists by virtue of effects on other pro-fibrotic LPA receptors. ATX expression is increased in the lungs of IPF patients where expression is detected in the hyperplastic bronchiolar epithelium and the alveolar epithelium surrounding the fibroblastic foci, as well as in fibroblast-

like cells and alveolar macrophages within the fibrotic interstitium (Oikonomou et al., 2012). However, despite an increase in ATX activity in bronchoaveolar lavage fluid (BALF) from bleomycin-instilled mice, the role of ATX in the pathogenesis of pulmonary fibrosis remains controversial. In one study, conditional genetic deletion of ATX from pulmonary epithelial cells or macrophages resulted in a reduction in fibrosis that was confirmed through pharmacological inhibition with the uncharacterized ATX inhibitor GWJ-A-3 (Oikonomou et al., 2012). However, in a more recent study, a well-characterized ATX inhibitor, PAT-048, was ineffective at reducing bleomycin-induced lung fibrosis despite virtually complete inhibition of ATX in plasma and BALF (Black et al., 2016). The lack of effect of PAT-048 was attributed to the fact that local production of LPA in the lung after bleomycin instillation is mediated by an ATX-independent, PLA_1-dependent pathway. Although the discrepancy between these studies is uncertain, it is clear that non-ATX dependent pathways for LPA generation exist and therapeutic approaches to target LPA generation will require identification of the enzyme(s) responsible in each disease/tissue setting.

In addition to its proposed role in pulmonary fibrosis, ATX has been implicated in other fibrotic diseases, particularly liver fibrosis. Serum ATX activity is increased in a rat CCl_4 model of liver fibrosis and correlates with fibrosis grade (Watanabe et al., 2007b), and a number of studies have demonstrated correlations between serum ATX protein/activity and human liver disease. In chronic hepatitis C patients, serum ATX is increased and shows positive correlations with serum hyaluronic acid (HA) and the histological stage of liver fibrosis (Watanabe et al., 2007a; Nakagawa et al., 2011). Serum ATX also showed a positive correlation with tissue stiffness, a marker of liver fibrosis, and serum ATX levels were shown to be a good predictor of cirrhosis (Nakagawa et al., 2011). In hepatocellular carcinoma (HCC) patients, serum ATX

strongly correlated with parameters of liver fibrosis, including serum HA, liver stiffness and aspartate aminotransferase/platelet ratio index (Kondo et al., 2014). A second group confirmed the correlation of elevated serum ATX with the severity of fibrosis in cirrhosis patients and further showed that high ATX levels independently associate with shorter overall survival (Pleli et al., 2014). However, ATX is rapidly cleared from the circulation through the liver sinusoidal endothelial cells and elevated serum ATX might reflect decreased clearance by a damaged, fibrotic liver (Jansen et al., 2009). Despite the considerable amount of correlative data supporting a role for ATX in the pathogenesis of liver disease and the availability of numerous small molecule inhibitors of ATX, there is currently no published data demonstrating efficacy of ATX inhibitors in animal models of liver disease. This is due, in part, to the fact that many ATX inhibitors have poor physicochemical properties that limit *in vivo* evaluation.

In this study, we describe the preclinical pharmacological, pharmacokinetic (PK) and pharmacodynamic (PD) properties of a novel small-molecule ATX inhibitor [3-((6-chloro-2-cyclopropyl-1-(1-ethyl-1H-pyrazol-4-yl)-7-fluoro-1H-indol-3-yl) thio)-2-fluorobenzoic acid sodium salt] (PAT-505) and evaluate the efficacy of this molecule in two different mouse models of NASH. PAT-505 is a potent, selective, non-competitive inhibitor that maximally inhibits ATX activity both in the plasma and in liver tissue after oral administration. When dosed therapeutically, PAT-505-treated animals showed a significant reduction in liver fibrosis in two mouse models of NASH. These data are the first to demonstrate a causal role for ATX in liver fibrosis and suggest that selective ATX inhibition may represent a novel therapy for the treatment of fibrotic liver diseases, including NASH.

JPET Fast Forward. Published on October 17, 2016 as DOI: 10.1124/jpet.116.237156
This article has not been copyedited and formatted. The final version may differ from this version.

Materials and Methods

Chemicals. PAT-505 (Fig. 1A) and three reference ATX inhibitors, PF-8380 (3,5-dichlorobenzyl 4-(3-oxo-3-(2-oxo-2,3-dihydrobenzo[d]oxazol-6-yl)propyl)piperazine-1-carboxylate) (Fig. 1B) (Gierse et al., 2010), GLPG1690 (2-((2-ethyl-6-(4-(2-(3-hydroxyazetidin-1-yl)-2-oxoethyl)piperazin-1-yl)-8-methylimidazo[1,2-a]pyridin-3-yl)(methyl)amino)-4-(4-fluorophenyl)thiazole-5-carbonitrile) (US2014/0303140; compound 2) (Fig. 1C) and PAT-048 (3-[6-chloro-7-fluoro-2-methyl-1-(1-propyl)-1*H*-pyrazol-4-yl-1*H*-indol-3-ylsulfanyl]-2-fluoro-benzoic sodium salt) (Black et al., 2016) (Fig. 1D) were synthesized at PharmAkea, Inc. For all *in vitro* studies using these test compounds, stock concentrations of 25 mM in dimethylsulfoxide (DMSO) were diluted to the final desired concentration in assay buffer. Carbon tetrachloride (CCl_4), olive oil, methylcellulose, 4-AAP (4-aminoantipyrine), TOOS (N-ethyl-N-(2-hydroxy-3-sulfopropyl-m-toluidine), HRP (Horse radish peroxidase), choline oxidase, pNP-TMP (thymidine 5'-monophosphate p-nitrophenyl ester), phenylmethylsulfonylfluoride (PMSF), aprotinin, and triton X-100 were all purchased from Sigma Aldrich (St. Louis, MO). 14:0 LPC (1-myristoyl-2-hydroxy-*sn*-glycero-3-phosphocholine) and 17:0 LPA (1-heptadecanyl-2-hydroxy-*sn*-glycero-3-phosphate sodium salt) were purchased from Avanti Polar Lipids (Alabaster, AL). Calf intestine alkaline phosphatase was purchased from Roche Diagnostics Corporation (Indianapolis, IN) and taurocholic acid was purchased from EMD Millipore (Billerica, MA).

***In vitro* LysoPLD Screening Assays.** Enzyme kinetics and concentration response curves of ATX inhibitors were evaluated using the lysoPLD TOOS assay. LysoPLD activity was measured in concentrated conditioned medium from Hep 3B2.1-7 cells (ATCC® HB-8064) (for concentration response curves), or conditioned medium from 293T/17 cells [HEK-293T/17]

(ATCC® CRL-11268) transiently transfected with ATXβ (for Michaelis-Menten kinetics) by measuring the release of choline from the substrate, 14:0 LPC, using the TOOS reagent as described previously (Stein et al., 2015). For determination of the appropriate IC_{50} value for the Michaelis-Menten kinetic studies, a concentration response curve of PAT-505 was first run using conditioned media from 293T/17 cells transiently transfected with ATXβ and 100 μM 14:0 LPC. The IC_{50} value from this study was determined to be 1.5 nM, therefore, substrate curves were generated in the presence of 0.75 nM (0.5X), 1.5 nM (1X), 3 nM (2X) and 6 nM (4X) PAT-505.

***In vitro* human blood/mouse plasma lysoPLD Assay.** *In vitro* lysoPLD inhibition in human blood or mouse plasma was evaluated by measuring the generation of 20:4 LPA from endogenous LPC. The human blood and mouse plasma assays have been described previously (Stein et al., 2015; Black et al., 2016). The concentrations of 20:4 LPA in the baseline sample from each assay were set to 0% and the concentrations of 20:4 LPA in the vehicle-treated 4 h incubated sample were set to 100%. The percent of produced 20:4 LPA from drug treated samples was then calculated relative to the baseline (0%) and vehicle-treated (100%) controls.

ENPP Counterscreening Assays. ***ENPP1/ENPP3 Assays***. ENPP1 and ENPP3 activities were evaluated by measuring the release of para-nitrophenyl from the chromogenic substrate, pNP-TMP (Levesque et al., 2007). Protein lysates from HEK 293T/17 cells transiently transfected with either an ENPP1 or ENPP3 expression vector using Lipofectamine® 2000 (Thermo Fisher Scientific) were prepared by harvesting cells 40-48 h after transfection followed by resuspension in ice-cold Harvest Buffer (*ENPP1*: 95 mM NaCl, 45 mM Tris pH 7.5, 0.1 mM PMSF and 10 μg/mL aproptinin or *ENPP3*: 20 mM Tris, 5 mM $MgCl_2$, pH 9.6) and sonication. Lysate was clarified by centrifugation at 300 x g for 10 min at 4°C and total protein content was determined using the Pierce BCA Protein Assay Kit (Thermo Fisher Scientific). To assay for ENPP activity,

JPET Fast Forward. Published on October 17, 2016 as DOI: 10.1124/jpet.116.237156
This article has not been copyedited and formatted. The final version may differ from this version.

2-3 µg of protein lysate was added to Assay Buffer (*ENPP1*: 50 mM Tris, pH 8.0, 140 mM NaCl, 1 mM $CaCl_2$, 5 mM KCl or *ENPP3*: 20 mM Tris, 5 mM $MgCl_2$, pH 9.6) and 2 µl of 50X test compound (in DMSO) in a total volume 100 µL in a 96-well plate. Incubation with test compound was carried out for 15 min at 37°C before the addition of 10 µL of 500 µM pNP-TMP (ENPP1) or 1 mM pNP-TMP (ENPP3). The plate was mixed and immediately transferred to a SpectraMax microplate reader (Molecular Devices, Sunnyvale, CA) and read at 410 nm every 15 sec for a total of 10 min at 37°C (ENPP1) or every 1 min for a total of 30 min at 37°C (ENPP3). ENPP Activity was calculated from the initial slope of the line. ***ENPP6 Assay.*** The ENPP6 assay is based on the ability of ENPP6 to hydrolyze LPC to form monoacyl glycerol and phosphorylcholine (Sakagami et al., 2005). Addition of alkaline phosphatase to the reaction results in the release of choline from the phosphorylcholine, which can then be measured using TOOS reagent. Protein lysate from HeLa cells (ATCC® CCL-2™) transiently transfected with an ENPP6 expression vector using Lipofectamine® 2000 was prepared by harvesting cells 40-48 h after transfection followed by resuspension in ice-cold Harvest Buffer (95 mM NaCl, 45 mM Tris, pH 7.5, 0.1 mM PMSF, 10 µg/mL aprotinin). Cells were sonicated to lyse and centrifuged at 300 x g for 10 min at 4°C to clarify the lysate prior to determination of protein content using the Pierce BCA Protein Assay Kit. To assay for ENPP6 activity, 5 µg of protein lysate was added to Assay Buffer (100 mM Tris, pH 9, 500 mM NaCl, 0.5% triton X-100) and 1 µL of 100X test compound (in DMSO) in a total volume of 100 µL in a 96-well plate. Incubation with test compound was carried out for 15 min at 37°C before the addition of 0.5 µL of 2U/µL Calf Intestine Alkaline Phosphatase (Roche Life Science, Indianapolis, IN) and 10 µL of 5 mM 14:0 LPC and further incubation for 1 h at 37°C. Following the 1 h incubation, 100 µL of TOOS detection mix (4.5 mM 4-AAP, 2.7 mM TOOS, 21U/mL HRP and 3U/mL choline oxidase in 50

mM Tris pH 8.0, 4.5 mM $MgCl_2$) was added to each well and incubated at room temperature for 15 min. The absorbance of the plate was measured at 555 nm using a SpectraMax microplate reader and choline concentrations determined from a choline standard curve. ***ENPP7 Assay.*** The ENPP7 assay is based on the ability of ENPP7 to hydrolyze LPC to form monoacyl glycerol and phosphorylcholine (Sakagami et al., 2005). Addition of alkaline phosphatase to the reaction resulted in the release of choline from the phosphorylcholine, which was then measured using Amplex® Red Reagent (Thermo Fisher Scientific). Conditioned medium from HEK 293T/17 cells transiently transfected with an ENPP7 expression vector using Lipofectamine® 2000 was prepared by removing the media containing the transfection mix 7 h after transfection, washing the cells with PBS and adding phenol-red-free DMEM. Cells were cultured an additional 40-48 h prior to harvesting the conditioned medium. Conditioned medium was centrifuged at 300 x g for 5 min at 4°C prior to concentration using Centricon® Plus-70 (10,000 NMWL) (EMD Millipore, Billerica, MA). To assay for ENPP7 activity, 2.5 µL of concentrated, conditioned media is added to Assay Buffer (50 mM Tris, pH 8, 150 mM NaCl and 10 mM taurocholic acid) and 2 µL of 50X test compound in a total volume of 60 µL in a black-wall, clear-bottom 96-well plate. Incubation with test compound was carried out for 15 min at 37°C before the addition of 20 µL of 0.5 mM 14:0 LPC (in Assay Buffer) and 20 µL of Amplex Red mix (50 µM Amplex® Red Reagent, 0.5 U/mL choline oxidase, 5 U/mL HRP and 20 U/mL calf intestine alkaline phosphatase in Assay Buffer). The plate was mixed well and immediately placed on a FlexStation 3 (Molecular Devices, Sunnyvale, CA) and read at excitation= 571 nm and emission= 585 nm every 2 min for a total of 1h at 37°C. Activity of ENPP7 was calculated from the initial slope of the line

PPAR Counterscreening. PAT-505 was screened for agonism and antagonism of PPARγ and PPARα ligand-dependent coactivator recruitment using the Lanthascreen® TR-FRET PPAR Coactivator Assay Kits according to the manufacturer's instructions (Thermo Fisher Scientific). GW1929 (Tocris/Bio-Techne, Minneapolis, MN) was used as a reference PPARγ agonist, GW7647 (Sigma Aldrich, St. Louis, MO) was used as a reference PPARα agonist and GW9662 (Cayman Chemical, Ann Arbor, MI) was used as reference PPARγ/PPARα antagonist.

Counterscreening. PAT-505 was screened at 10 μM in duplicate for inhibition of radiolabeled agonist or antagonist binding to a panel of 55 human receptors/channels at Eurofins Cerep Panlabs (France) according to Eurofins Standard Operating Procedure.

Crystal Structure. Methods for the recombinant expression and purification of human ATX and methods for the crystallography have been described previously (Stein et al., 2015).

Animals. Female and male C57BL/6 and BALB/c mice (Charles River, 6-9 weeks, at study initiation) were used for the PK and efficacy studies. Animals were given free access to food and water and maintained on a 12 h light/dark schedule. All procedures were approved by the local Institutional Animal Care and Use Committee and carried out in accordance with the National Institutes of Health *Guide for the Care and Use of Laboratory Animals.*

Plasma Pharmacokinetics (PK) and Pharmacodynamics (PD). The pharmacokinetics of PAT-505 were determined in fed female C57BL/6 mice and fasted male Sprague-Dawley rats. PAT-505 was administered either intravenously as a solution in 0.9% saline at doses of 5 mg/kg (mouse) or 0.2 mg/kg (rat) via a bolus injection into the tail vein (mouse) or jugular vein (rat) or orally as a solution in 0.5% methylcellulose (MC) at doses of 30 mg/kg (mouse) or 10 mg/kg (rat). For mice, animals were anesthetized with isofluorane and a terminal cardiac puncture was

performed at various times between 0.5 and 24 h post oral dose (n=3 animals per time-point). For rats, serial blood samples were taken from each rat via the jugular vein at various times between 0.5 and 24 h post oral dose (n=3 animals per time-point). Blood was collected into EDTA vacutainer tubes and centrifuged at 800 x g for 10 min at 4°C to isolate plasma. Analysis of PAT-505 plasma concentrations was performed using liquid chromatography mass spectrometry (LC/MS) as follows. Known amounts of PAT-505 were added to naïve mouse/rat plasma to yield a standard curve from 1 to 5000 ng/mL. 30 µL plasma samples were precipitated using 150 µL of 70:30 acetonitrile:methanol containing another proprietary small molecule with a distinct mass to charge as the internal standard. The supernatant (150 µL) was mixed with 100 µL water then centrifuged at 4000 x g for 10 min at 4°C. The analyte mixture (10 µL) was injected with a PAL autosampler (Leap Technologies, Carrboro, NC, USA). Calibration curves were constructed by plotting the peak-area ratio against the known concentrations. The lower limit of quantitation was 1 ng/mL. The data were subjected to quadratic regression analysis with $1/x^2$ weighting. ATX lysoPLD activity after oral dosing was evaluated in 10 µL plasma using the lysoPLD TOOS assay and a 2-4 h 37°C incubation with 2 mM 14:0 LPC as described elsewhere (Stein et al., 2015). ATX lysoPLD activity from vehicle treated animals was set to 100% and the % activity in the drug treated animals was calculated relative to this control.

Acute Mouse CCl_4 Pharmacodynamic (PD) Assay. Male BALB/c mice were given a single intraperitoneal administration of 25% CCl_4 in olive oil at 0.8 mL/kg. PAT-505 dosed at 30 mg/kg was administered orally in 0.5% MC at 2 or 16 h prior to sacrifice for evaluation of ATX inhibition at approximately peak and trough (Fig. 2A). Animals were sacrificed 24 hours post CCl_4 administration and plasma and liver collected for evaluation of ATX activity. Livers were flash frozen in liquid nitrogen and kept at -80°C until use. Compound concentrations and

lysoPLD activity in the plasma were determined as described above. For determination of compound concentration and lysoPLD activity in liver, livers were homogenized in lysoPLD buffer (100 mM Tris, pH 9, 500 mM NaCl, 5 mM $MgCl_2$, 5 mM $CaCl_2$ and 0.05% triton X-100) at 200 mg liver/mL then sonicated 1 min before centrifuging for 10 min at 16,000 x g for 10 minutes at 4°C. Protein concentration of the supernatant was determined using the BCA Protein Assay Kit (Thermo Fisher) and an albumin standard curve. Samples were diluted to 5 mg/mL and ATX lysoPLD activity was determined by calculating the concentration of 14:0 LPA generated from the substrate, 14:0 LPC as follows: 95 µL of the 5 mg/mL supernatant was added to 5 µL of 10 mM 14:0 LPC for a final concentration of 500 µM LPC. Samples were incubated at 37°C for 24 hours followed by analysis of 14:0 LPA by LC/MS as follows. A 5 mg/mL stock solution of 14:0 LPA in chloroform was diluted serially in methanol to generate stock solutions ranging from 10 to 50,000 ng/mL. To generate the standard curve, 3 µL of each stock solution was added to 27 µL of naïve mouse liver homogenate to yield a standard curve from 1 to 5000 ng/mL. 150 µL of methanol containing 17:0 LPA as the internal standard was added to each standard and to a 30 µL aliquot of each liver homogenate sample. The supernatant (150 µL) was mixed with 100 µL water then centrifuged at 4000 x g for 10 min at 4°C. The analyte mixture (10 µL) was injected with a PAL autosampler (Leap Technologies, Carrboro, NC, USA). Calibration curves were constructed by plotting the peak-area ratio against the known concentrations. The lower limit of quantitation was 1 ng/mL. The data were subjected to linear regression analysis with $1/x^2$ weighting. For measurement of PAT-505 concentrations in liver tissue, liver samples were diluted with 4 volumes of PBS (wt./vol.) and homogenized using an OMNI Bead Ruptor 24 (OMNI International, Kennesaw, GA) . Standards were prepared by serial diluting PAT-505 into naïve mouse liver homogenate. 200 µL of 70:30

acetonitrile:methanol containing PAT-506 [3-((6-chloro-2-cyclopropyl-1-(1-methyl-1H-pyrazol-4-yl)-7-fluoro-1H-indol-3-yl) thio)-2-fluorobenzoic acid sodium salt; the N-methylpyrazole analog of PAT-505] as an internal standard was added to 30 µL liver homogenate. Samples were mixed for 5 min, and then centrifuged at 4000 x g for 10 min to pellet precipitated protein. 150 µL of the supernatant was removed and diluted with 100 µL of water before analysis by HPLC-MS as described above. Area ratio (PAT-505 to internal standard) response of samples was compared with the response generated from the standard curve. Analytical range was 50 – 12,500 ng/mL.

Mouse STAM™ Liver Fibrosis Model. Mouse Stelic Animal Model (STAM™) of NASH was performed at Stelic Institute & Co (Japan). Briefly, NASH was induced in male C57BL/6 mice by a subcutaneous injection of 200 µg streptozotocin solution (Sigma Aldrich, USA) two days after birth and then feeding a high fat diet (57% kcal% fat Cat# HFD32, CLEA Japan, Japan) starting at 4 weeks of age. At 6 weeks of age, mice were randomized and treated with 10 or 30 mg/kg PAT-505 in 0.5% MC or vehicle twice daily until 12 weeks of age (n=8/group) (Fig. 2B). Telmisartan (Micardis®, Boehringer Ingelheim, Germany), dosed once daily at 5 mg/kg in water, was used as a positive control (n=6/group). At the end of the study, the mice were sacrificed and blood collected into EDTA vacutainer tubes for preparation of plasma used in the analysis of drug concentrations and ATX lysoPLD activity as described above. Non-fasting whole blood glucose was measured in whole blood using LIFE CHECK (EIDIA, Japan). Liver was collected for analysis of liver weight, triglyceride content and liver histology. Liver total lipids were obtained by Folch's method (Folch et al., 1957). Liver samples were homogenized in chloroform-methanol (2:1, v/v) and incubated overnight at room temperature. After washing with chloroform-methanol-water (8:4:3, v/v/v), the extracts were evaporated to dryness and

dissolved in isopropanol. Liver triglyceride content was measured by Triglyceride E-test (Wako Pure Chemical Industries, Japan). Liver histology was evaluated on sections cut from paraffin blocks of liver tissue pre-fixed in Bouin's solution and stained with Lillie-Mayer's Hematoxylin (Muto Pure Chemicals, Japan) and eosin (Wako Pure Chemical Industries, Japan) or picro-Sirius red (PSR) (Waldeck, Germany). NAFLD Activity score (NAS) was calculated according to the criteria of Kleiner (Kleiner et al., 2005). To visualize collagen deposition, liver sections were stained with PSR and fibrosis areas was quantitated using bright field images of PSR stained sections captured around the central vein using a digital camera (DFC280; Leica, Germany) at 200-fold magnification. The positive areas in 5 fields/section were measured using ImageJ software (National Institutes of Health, USA).

Mouse CDAHFD NASH Liver Fibrosis Model. NASH was induced in male C57BL/6 mice according to the method of Matsumoto (Matsumoto et al., 2013). Briefly, 5-week-old mice were acclimated for 1 week on normal chow (NC) prior to switching to a choline-deficient, L-amino acid-defined, high-fat diet (CDAHFD) (Research Diets Cat# A06071302) containing 60% kcal% fat and 0.1% methionine. Animals were fed CDAHFD for 5 weeks before randomization into treatment groups (n=7-10 per group). Vehicle or PAT-505 (3-30 mg/kg) was administered by oral gavage in 0.5% MC once daily from week 5 to week 12 (Fig. 2C). At week 12, the mice were fasted for 4 hours prior to sacrifice. Blood was collected into EDTA vacutainer tubes and plasma prepared for the analysis of drug concentrations and ATX lysoPLD activity as described above. Serum was collected for the analysis of liver enzymes (ALT, AST, ALP, bilirubin) at Stat Veterinary Lab (San Diego, CA) using a Beckman Coulter AU480 chemistry analyzer. Liver was collected for the analysis of liver weights then a portion snap frozen and stored at -80°C for subsequent analysis of liver triglycerides. Another portion of the liver was fixed overnight in

10% neutral buffer formalin then transferred to 70% ethanol to process for histology. Liver triglycerides were measured using a colorimetric Liver triglyceride kit (Abcam, Cambridge, UK). Briefly, 100 mg liver tissue was homogenized in 1 mL 0.5% NP-40 and then the samples slowly heated to 100°C for 5 min before cooling to room temperature. The heating process was repeated then the samples centrifuged at 16,000 x g for 2 min. The supernatant was removed and diluted 1:100 prior to assaying 20 µL using the kit and following the manufacturer's instructions.

Histological analysis. For histological analysis, liver sections were stained with H&E or PSR at Seventh Wave Laboratories (St. Louis, MO) using their standard techniques. The H&E-stained sections were shuffled together, examined microscopically, and sorted into categories of steatosis (0, 1, 2, or 3) while blinded to the group designation and animal number. After this sorting was completed, the slide label was examined and steatosis, inflammation, and hepatocyte ballooning were recorded. The NAS score represents the composite of the steatosis, inflammation, and hepatocyte ballooning scores. The PSR-stained sections were shuffled together, examined microscopically, and fibrosis score (0, 1, 2, 3, or 4) recorded while blinded to the group designation and animal number. α-SMA immunohistochemistry was performed using Abcam antibody ab5694 according to standard techniques at Seventh Wave Laboratories. α-SMA staining was scored as 0=no increase, 1=minimally increased or 2= mild.

Statistical Analysis. Statistical analyses were performed using Bonferroni or Dunnett's Multiple Comparison Test on GraphPad Prism 6 (GraphPad Software, USA). *P* values <0.05 were considered statistically significant. A trend was assumed when a one-tailed t-test returned *P* values <0.05. *In vivo* results are expressed as mean ± SEM. Because the IC_{50} values from the *in vitro* results are log-based values, the average data is expressed as the geometric mean of the IC_{50} values and the geometric standard deviation.

Results

***In Vitro* Potency, Selectivity and Mode of Inhibition.** The potency of PAT-505 against the lysoPLD activity of human ATX was determined using 14:0 LPC as a substrate and conditioned media from the hepatocellular carcinoma cell line, Hep3B, which secretes high concentrations of ATX. PAT-505 displayed potent, concentration-dependent inhibition of ATX lysoPLD activity with an average IC_{50} value of 2.0 nM (Figure 3A, Table 1). This potency is similar to that of the published ATX inhibitors, PF-8380 and PAT-048, which have average IC_{50} values of 7.1 nM and 1.1 nM, respectively and is significantly more potent than that of GLPG1690 (average IC_{50} value of 180 nM), a compound currently in clinical development for IPF (Fig. 3A, Table 1). PAT-505 is selective for ATX versus other ENPP proteins as 10 μM PAT-505 resulted in less than 10% inhibition of ENPP1, 3, 6 and 7 (Supplementary Table 1). Because LPA has been shown to bind and activate peroxisome proliferator-activated receptor γ (PPARγ) (McIntyre et al., 2003), we screened PAT-505 for agonism and antagonism of PPARγ and PPARα ligand-dependent coactivator recruitment. At concentrations up to 30 μM, PAT-505 displayed no significant agonist or antagonist activity at PPARα and no significant agonist activity at PPARγ (Supplementary Table 2 and data not shown). However, PAT-505 did inhibit ligand-dependent coactivator recruitment of PPARγ by 62-122% at concentrations ranging from 10-100 μM (Supplementary Table 2). Finally, PAT-505 was screened for binding to a panel of 55 other human proteins, including receptors and channels, and showed no significant binding to the majority of the proteins. However, PAT-505 did display marginal inhibition of radiolabeled agonist or antagonist binding to the adenosine A3 receptor, MT1 melatonin receptor, prostaglandin E2 EP4 receptor, 5-HT5a serotonin receptor and GABA-gated Cl- channel with 50-70% inhibition at 10 μM (data not shown).

JPET Fast Forward. Published on October 17, 2016 as DOI: 10.1124/jpet.116.237156
This article has not been copyedited and formatted. The final version may differ from this version.

While PAT-505 displayed potent inhibition of ATX in the context of conditioned media, measurement of potency in blood is often regarded as the best predictor of *in vivo* potency, as many small molecules display substantial binding to albumin or other blood proteins that can significantly affect target protein binding and reduce inhibitory activity. Therefore, to more accurately estimate *in vivo* potency, we evaluated the ability of PAT-505 to inhibit lysoPLD activity in blood or plasma. In the context of human blood, PAT-505 maintained good potency with an average IC_{50} value of 9.7 nM and an average IC_{90} value of 96 nM for inhibition of lysoPLD activity. In this physiological matrix, only PAT-048, with an average IC_{50} value of 8.9 nM, showed similar potency to PAT-505, whereas both PF-8380 and GLPG1690 were significantly less potent than PAT-505, displaying average IC_{50} values of 280 nM and 82 nM, respectively (Fig. 3B, Table 1). To obtain a more accurate estimation of *in vivo* potency in our preclinical efficacy species, PAT-505 was evaluated in a mouse plasma assay. In mouse plasma, PAT-505 inhibited ATX lysoPLD activity with an average IC_{50} value of 62 nM and an average IC_{90} value of 630 nM, while PAT-048, PF-8380 and GLPG displayed average IC_{50} values of 22, 320, and 360 nM, respectively (Fig. 3C, Table 1).

A number of inhibitor binding sites have been identified in the ATX protein using X-ray crystallography, including both competitive and non-competitive sites (Stein et al., 2015). To determine the mode of enzyme inhibition for PAT-505, substrate/velocity curves of lysoPLD activity were generated in the presence of varying concentrations of inhibitor and the effects on K_m and V_{max} plotted. Increasing concentrations of PAT-505 resulted in a significant decrease in V_{max}, with only a very minor effect on K_m, and an alpha value of approximately 2.5, all of which are consistent with a primarily non-competitive mode of inhibition (Fig. 3D,E). The enzyme kinetic data is supported by crystal structure data which shows that PAT-505 binds to human

JPET Fast Forward. Published on October 17, 2016 as DOI: 10.1124/jpet.116.237156
This article has not been copyedited and formatted. The final version may differ from this version.

ATX in an allosteric site adjacent to the catalytic site which had been identified previously as a hydrophobic channel (Supplementary Fig. 1A) (accession code 5KXA) (Nishimasu et al., 2011). Not surprisingly, PAT-505 overlays well with the crystal structure of the non-competitive ATX inhibitor, PAT-347, which was also crystallized with human ATX and found to bind exclusively in the hydrophobic channel (Supplementary Fig. 1b) (Stein et al., 2015).

Pharmacokinetic/pharmacodynamic Profile in Mouse and Rat. The pharmacokinetics (PK) of PAT-505 were assessed in female C57BL/6 mice and male Sprague-Dawley rats after intravenous (i.v) and oral (p.o) administration. After intravenous administration of PAT-505, clearance values (Cl_{Pl}) in mouse and rat were 2.0 and 0.22 mL/min/kg, respectively, which suggests very low clearance with respect to liver blood flow (Table 2). Volume of distribution (VDss) was higher in mouse (0.41 L/kg) compared to rat (0.16 L/Kg). Plasma half-life ($t_{1/2}$) was longer in rat (10.2 hours) compared to mouse (3.9 hours) which is consistent with the clearance values (Table 2). After oral administration in mouse and rat, PAT-505 reached maximum plasma concentrations (C_{max}) of 22.7 µg/mL (48 µM) and 33.9 µg/mL (70.0 µM), respectively, and showed good bioavailability (52-57%) (Supplementary Fig. 2 and Table 2). Dose adjusted exposure (Dose adjusted AUC) was approximately seven-fold higher in rat compared to mouse (33.8 vs. 4.9), again consistent with the lower clearance in rat.

The ability of PAT-505 to inhibit plasma ATX activity was assessed in the PK samples from the oral dosing studies using the lysoPLD TOOS assay. In mice, PAT-505 treatment resulted in an average 60% inhibition of plasma ATX activity at 0.5 h post-dose which then increased to 85-90% inhibition from 1-8 h post-dose (Fig. 4A). Even at 16 and 24 h post-dosing, plasma ATX activity was approximately 70% inhibited which correlates well with the plasma concentrations of PAT-505 remaining near the mouse plasma IC_{90} value (~630 nM) at these late

JPET Fast Forward. Published on October 17, 2016 as DOI: 10.1124/jpet.116.237156
This article has not been copyedited and formatted. The final version may differ from this version.

time points. In rat, ATX activity was maximally inhibited after oral administration (≥ 90%) at all time points collected, consistent with the plasma concentrations of PAT-505 above the rat plasma IC_{90} for all time points analyzed (Fig. 4B).

Inhibition of ATX Activity in Liver (Acute CCl_4 model). The ability of PAT-505 to inhibit ATX lysoPLD activity in liver tissue was evaluated after administration of CCl_4. ATX lysoPLD activity is extremely low in normal liver tissue homogenate, however, intraperitoneal injection of CCl_4 to male BALB/c mice results in a 6-fold increase in lysoPLD activity in liver homogenate (Fig. 5A). Additionally, CCl_4 injection results in a small, but significant, 1.5-fold increase in ATX lysoPLD activity in plasma (Fig. 5B). PAT-505 dosed at 30 mg/kg either 2 h or 16 h prior to harvest resulted in a ≥90% decrease in ATX lysoPLD activity bringing values back to baseline activity in the liver and reducing values to well below the baseline in the plasma (Fig. 5A, B). Plasma and liver tissue drug concentrations were above the *in vitro* mouse plasma assay IC_{90} value (~630 nM) for all animals at both the 2 h and 16 h timepoints (data not shown).

Mouse STAM™ Liver Fibrosis Model. The effect of PAT-505 on the development of hepatic steatosis, inflammation and fibrosis was first assessed in the mouse STAM™ model of NASH. In this model, NASH is induced by a single subcutaneous injection of streptozotocin two days after birth followed by high-fat diet feeding at approximately four weeks of age. The angiotensin II receptor antagonist, telmisartan, is used as a positive control. PAT-505 dosed from week 6 to 12 had no significant effect on mean body weight, liver weight;body weight ratio or liver enzymes (Supplementary Fig. 3A-D). Telmisartan treatment had no significant effect on liver enzymes, but resulted in a statistically significant reduction in liver weight:body weight ratio (Supplementary Fig. 3A-D). There were no significant differences in whole blood glucose

concentrations between the vehicle group and any of the treatment groups (Supplementary Fig. 3F).

Histological analyses of H&E stained liver sections showed moderate to severe micro- and macrovesicular fat deposition, hepatocellular ballooning and inflammatory cell infiltration in the vehicle-treated animals (Supplementary Fig. 4). The telmisartan and PAT-505 groups showed improvements in hepatocellular ballooning and inflammatory cell influx, but only the telmisartan group showed an improvement in steatosis and liver triglycerides (Fig.6C and Supplementary Fig.3E and 4). The 10 mg/kg dose of PAT-505 had no significant effect on steatosis, but showed a trend for reduction in liver triglycerides and overall showed a statistically significant improvement in NAFLD activity score (NAS) (Fig. 6C, D and Supplementary Fig. 3E). In contrast, the 30 mg/kg PAT-505 dose showed a trend for increased steatosis and liver triglycerides and, as a result, showed no significant difference in NAS from the vehicle group, despite the reduction in hepatocellular ballooning and inflammatory cell influx (Fig. 6C, D and Supplementary Fig. 3E and 4).

Histological analyses of PSR stained liver sections showed collagen deposition in the pericentral region of the liver lobule (Supplementary Fig. 5). There was a small but significant decrease in fibrotic area in the 10 mg/kg PAT-505 and telmisartan groups; the 30 mg/kg PAT-505 group showed a trend for a decrease in fibrotic area that did not reach statistical significance (Fig. 6E and Supplementary Fig. 5).

Mouse CDAHFD Model of NASH. The effect of PAT-505 on the development of hepatic steatosis, inflammation and fibrosis was assessed in a second mouse model of NASH that was induced by feeding a choline-deficient diet containing 0.1% methionine and high-fat (60 kcal%

fat) (CDAHFD) (Matsumoto et al., 2013). In the first study, PAT-505 was dosed orally once daily at 3, 10 or 30 mg/kg from week 5-12. Histological analyses of H&E stained liver sections showed moderate to severe macrovesicular fat deposition, moderate inflammatory cell infiltration and occasional ballooned hepatocytes in the vehicle treated animals (Supplementary Fig. 6A-D). Livers from all vehicle-treated mice fed CDAHFD showed perisinusoidal and portal/periportal bridging fibrosis scored as grade 3, with approximately 7.5% of the area PSR positive and minimally increased α-SMA immunostaining (Supplementary Fig. 6D-G). PAT-505 treatment had no significant effect on body weight, liver weight, hepatic inflammation or hepatocellular ballooning (Supplementary Fig. 6A-C and data not shown). However, treatment with the 30 mg/kg dose of PAT-505 showed a significant reduction in fibrotic score and % PSR positive area and a dramatic reduction in α-SMA immunoreactivity (Supplementary Fig. 6D-G). In contrast, there were no differences between the vehicle group and the 3 or 10 mg/kg PAT-505 treatment groups on fibrotic score or α-SMA immunoreactivity (Supplementary Fig. 6D-G). While there was no significant effect on steatotic score, microscopic examination of the 30 mg/kg PAT-505 group showed a small change in the character of the lipid vacuoles with smaller individual vacuoles in some hepatocytes characterized more as microvesicular steatosis as compared to the macrovesicular steatosis observed in the vehicle-treated animals (data not shown).

ATX lysoPLD activity was evaluated in the plasma samples taken 24 h after the last dose (trough) for determination of target coverage. Plasma ATX activity increased approximately 1.5-fold in the CDAHFD animals compared to the normal chow animals and was inhibited by an average of 70%, 76% and 90% after treatment with 3, 10 or 30 mg/kg PAT-505, respectively (Supplementary Fig. 7A). At the 30 mg/kg dose, trough concentrations of PAT-505 in the plasma

were above the average IC_{90} value from the *in vitro* mouse plasma assay for ~90% of the animals, whereas >50% of the animals in the 3 and 10 mg/kg treatment groups had trough plasma concentrations that were below the average IC_{90} value from the *in vitro* mouse plasma assay but above the average IC_{50} value (Supplementary Fig. 7B). Therefore, the % inhibition of ATX activity in the plasma shows a good correlation with the plasma PAT-505 concentrations. Trough concentrations of PAT-505 in liver tissue were also evaluated in the 10 and 30 mg/kg dose groups. As in the plasma, trough PAT-505 concentrations in liver tissue from the 30 mg/kg dose group were all above the *in vitro* mouse plasma IC_{90} value, whereas ~70% of the animals in the 10 mg/kg dose group had trough liver concentrations that were below the average IC_{90} value (Supplementary Fig. 7C).

Because only the 30 mg/kg PAT-505 dose resulted in maximal inhibition of trough plasma ATX activity and displayed anti-fibrotic activity in the first CDAHFD study, we performed a second study at the 30 mg/kg dose level. As in the first study, PAT-505 treatment had no significant effect on body weight, liver weight, hepatic inflammation or hepatocellular ballooning (Supplementary Fig. 8A-D). In contrast, PAT-505 treatment once again resulted in robust anti-fibrotic activity as 70% of the animals in the vehicle-treated group had fibrosis scores of grade 3, whereas 70% of the animals in the PAT-505 treated group had fibrosis scores of grade 1 (Fig. 7A,C). In addition, PAT-505 treatment resulted in a significant reduction in α-SMA immunoreactivity (Fig. 7B, D). Analysis of serum liver enzymes showed that PAT-505 treatment resulted in a significant reduction in total bilirubin and AST concentrations, with no significant effect on ALT or ALP concentrations (Fig. 7E, Table 3 and Supplementary Fig. 8F). As observed in the first study, there was no significant difference in steatosis score for 70% of the PAT-505-treated animals, however, 30% of the animals showed a significant reduction in the

severity of steatosis (Supplementary Fig. 8E). In addition, microscopic examination of the grade 3 animals in the PAT-505 treatment group again revealed more microvesicular steatosis as compared to the macrovesicular steatosis observed in the vehicle treated animals and this correlated with a small but significant reduction in liver triglycerides (Fig. 7A,F and Table 3). As expected, plasma ATX activity increased in the animals fed the CDAHFD and trough plasma activity was decreased by 90% with PAT-505 treatment, which correlated with all animals displaying trough plasma concentrations above the IC_{90} value from the *in vitro* mouse plasma assay (Fig. 7G,H). In addition, all animals in the treatment group also displayed trough liver PAT-505 concentrations above the IC_{90} value from the *in vitro* mouse plasma assay (Fig. 7H).

JPET Fast Forward. Published on October 17, 2016 as DOI: 10.1124/jpet.116.237156
This article has not been copyedited and formatted. The final version may differ from this version.

Discussion

Over the past several years a number of ATX inhibitors have been described in the literature, however, many of these inhibitors have had poor bioavailability and/or rapid clearance that limited *in vivo* characterization (Albers and Ovaa, 2012; Castagna et al., 2016). Here we describe PAT-505, a novel, potent and selective ATX inhibitor that demonstrates 24 hour maximal inhibition of ATX activity with once daily oral dosing. PAT-505 treatment exhibits a robust plasma PK/PD correlation that suggests *in vivo* potency is best predicted by *in vitro* potency in the blood/plasma assay. The strong correlation between plasma PAT-505 concentrations and ATX inhibition is also observed in the mouse efficacy studies where trough plasma concentrations above the *in vitro* mouse plasma IC_{90} (~630 nM), correlate with maximal 90% inhibition of ATX activity, whereas plasma drug concentrations between the *in vitro* mouse plasma IC_{50} and IC_{90} value show intermediate inhibition (70-76%). Based on this data and the *in vitro* human blood potency, PAT-505 is expected to be approximately 5-times more potent than the clinical compound, GLPG1690, which is currently the only ATX inhibitor that has progressed to clinical development (Castagna et al., 2016).

Because of the potential for ATX to contribute to obesity-related insulin resistance and inflammation (Rancoule et al., 2012; Bai et al., 2013; Sevastou et al., 2013; Rancoule et al., 2014; Reeves et al., 2015) and the strong correlation between serum ATX protein/activity and liver fibrosis in several patient populations (Watanabe et al., 2007a; Nakagawa et al., 2011; Kondo et al., 2014; Pleli et al., 2014), we focused on demonstrating anti-fibrotic efficacy in preclinical models of NASH. Non-alcoholic fatty liver disease is associated with obesity and insulin resistance and can lead to chronic inflammation/steatohepatitis and ultimately to fibrosis and advanced liver disease (Ratziu, 2016). Using PAT-505 dosing regimens that maximally

JPET Fast Forward. Published on October 17, 2016 as DOI: 10.1124/jpet.116.237156
This article has not been copyedited and formatted. The final version may differ from this version.

inhibit ATX activity in plasma and liver, we demonstrate anti-fibrotic efficacy in two distinct mouse models of NASH.

In the STAM™ model, PAT-505 treatment showed a small but significant reduction in collagen staining, although the extent of fibrosis in this model was mild and the reduction in %PSR positive area was significantly less than the positive control, telmisartan. Interestingly, PAT-505 treatment also showed reduced hepatic inflammation and hepatocellular ballooning, although these improvements were marginal and not as robust as telmisartan. However, the small changes in inflammation and ballooning in the 10 mg/kg dose group translated into a statistically significant reduction in NAS. Paradoxically, while the 10 mg/kg dose of PAT-505 had no effect on steatosis but trended to lower liver triglycerides, the 30 mg/kg dose trended to increase steatosis and liver triglycerides and this resulted in no significant reduction in NAS for the 30 mg/kg treatment group, despite the decrease in hepatic inflammation and hepatocellular ballooning. However, we note that the doses of PAT-505 administered in the STAM™ study were selected prior to the establishment of the acute CCl_4 PD assay and a BID dosing regimen was thought to be required for maintaining maximal inhibition between doses. However, trough plasma and liver drug concentrations analyzed at the end of the STAM™ study averaged 9.6 μM and 6.7 μM, respectively, which is ≥10-fold higher than the ~630 nM concentration required for maximal inhibition (Supplementary Fig. 7). Based on the PK, concentrations of PAT-505 are expected to be 20-48-fold higher than trough concentrations for the first 8 hours post-dosing, which translates into expected concentrations ranging from 130-320 μM. Therefore, we might expect off-target activity of PAT-505 that could contribute to the negative effects on steatosis. For example, at 10 μM PAT-505 showed 58% inhibition of ligand-dependent coactivator recruitment to PPARγ and 69% inhibition of radiolabeled agonist binding to the melatonin MT1

receptor and these proteins have been shown to regulate hepatic steatosis and triglyceride storage (Sun et al., 2015; Cave et al., 2016). Clearly, additional studies will be required to understand the connection between PAT-505 treatment and exacerbated hepatic steatosis.

In the CDAHFD model of NASH, 30 mg/kg PAT-505 treatment resulted in a dramatic reduction in fibrosis, despite the fact that the extent of fibrosis in this model was greater than that observed in the STAM™ model. In addition, robust anti-fibrotic efficacy was observed in the absence of any significant effect on hepatic inflammation or hepatocyte ballooning, demonstrating that effects on inflammation and hepatocyte ballooning are context dependent and likely not driving the anti-fibrotic efficacy. Importantly, doses of PAT-505 that resulted in less than maximal inhibition of plasma ATX activity and less then IC_{90} concentrations of PAT-505 in liver tissue at trough did not demonstrate anti-fibrotic efficacy, even though drug concentrations remained above the IC_{50} at trough. These data suggest that complete inhibition of ATX is required for efficacy in the CDAHFD model. The improvement in fibrosis in the CDAHFD model was supported by reductions in α-SMA staining, total serum bilirubin and AST concentrations. Interestingly, PAT-505 treatment resulted in a small, but significant, reduction in liver Tg and also had a mild effect on hepatic steatosis, with a larger area of microvesicular steatosis in the PAT-505-treated animals compared to macrovesicular steatosis in the vehicle-treated animals. However, these effects on steatosis are mild and unlikely to contribute significantly to the anti-fibrotic activity. Importantly, we observed no increase in steatosis with PAT-505 treatment in this model, which we attribute to the 3-10-fold lower trough drug concentrations in this study. Taken together, these data suggest ATX inhibition has direct anti-fibrotic effects in the liver, with little to no effect on hepatic inflammation, hepatocellular ballooning and steatosis. We also note that a distinct PharmAkea ATX inhibitor, structurally

very similar to PAT-505, was evaluated in a rat CDAA NASH model. Treatment with this compound resulted in robust attenuation of hepatic fibrosis, similar to the extent observed in the PAT-505 mouse CDAAHFD study, with no effect on hepatic inflammation, hepatocellular ballooning or steatosis (unpublished data), thus demonstrating robust anti-fibrotic efficacy of ATX inhibitors in two preclinical NASH models.

Hepatic stellate cell (HSC) activation is a central event in the development of hepatic fibrosis. The ability of PAT-505 to attenuate hepatic fibrogenesis suggests that ATX activity and downstream LPA signaling may regulate HSC biology. Indeed, others have shown that LPA modulates HSC morphology, gel contraction and adhesion to extracellular matrix in a Rho-kinase dependent manner (Yanase et al., 2000). In addition, LPA was shown to increase proliferation of primary rat HSCs (Ikeda et al., 1998). Interestingly, the same concentration of LPA that supported HSC proliferation was shown to exert an anti-mitogenic response on primary rat hepatocytes stimulated with either HGF or EGF (Ikeda et al., 1998). The identification of the LPA receptor(s) involved in regulating HSC and hepatocyte biology and the ability of ATX/LPA signaling to regulate other cell types involved in HSC activation, including sinusoidal endothelium and Kupffer cells, will require further research.

LPA-LPA1 signaling has been shown to contribute to the pathogenesis of fibrosis in multiple organ systems including the lung, kidney, skin and peritoneum (Pradere et al., 2007; Pradere et al., 2008; Tager et al., 2008; Swaney et al., 2010; Castelino et al., 2011; Swaney et al., 2011; Sakai et al., 2013). However, it is likely that locally produced LPA drives fibrosis progression and the role of ATX in localized LPA production in various disease settings remains uninvestigated or controversial. In the mouse bleomycin model of lung fibrosis, ATX expression is increased and thought to contribute to the development of pulmonary fibrosis since the

uncharacterized, small molecule ATX inhibitor, GWJ-A-23, attenuated fibrosis in this model (Oikonomou et al., 2012). However, more recently, PAT-048, a distinct and well-characterized small molecule ATX inhibitor, was ineffective at reducing bleomycin-induced lung fibrosis despite complete inhibition of ATX activity in plasma and BALF, and this was attributed to an ATX-independent mechanism for local pulmonary LPA production (Black et al., 2016). However, another potential explanation for these disparate results is that GWJ-A-23 may be able to penetrate a localized area of the lung where ATX-dependent LPA production is occurring, whereas PAT-048 is not. Clearly, non-ATX dependent pathways for LPA generation exist and therapeutic approaches to target LPA generation will require identification of the enzyme(s) responsible in each disease/tissue setting. Additionally, measurement of ATX inhibition in plasma is not a surrogate for local tissue inhibition and mechanisms to evaluate tissue inhibition should be investigated where possible. Here, we describe a method to assess ATX activity in the liver, our target tissue. We demonstrate that intraperitoneal administration of CCl_4 acutely increases ATX activity to measurable levels locally in the liver and we show a good correlation of PAT-505 liver concentrations with ATX inhibition. Interestingly, there is a much smaller increase in plasma ATX activity after CCl_4 administration and this may reflect a decrease in clearance of ATX from an acutely damaged liver. Importantly, this assay has allowed for the direct assessment of ATX inhibition vs. drug concentrations in liver tissue.

X-ray crystallography studies using human ATX have demonstrated both competitive and non-competitive/allosteric inhibitor binding sites within the ATX protein, with the allosteric site corresponding to the previously identified LPA binding hydrophobic channel (Nishimasu et al., 2011; Stein et al., 2015). The competitive binding site includes the Zn^{+2} containing active site and a hydrophobic pocket which accommodates the LPC tail (Hausmann et al., 2011; Nishimasu

et al., 2011). Many early ATX inhibitors were non-drug like, lipid-like structures that mimicked the substrate, LPC, and bound competitively in the active site (Castagna et al., 2016). To date, many published ATX inhibitors can be characterized as containing a lipophilic tail, core spacer and acidic head group, which presumably bind in a competitive manner. The lipophilic portion is accommodated in the hydrophobic pocket and the acidic head group interacts with the Zn^{+2} in the active site, as exemplified by the competitive inhibitor PF-8380 (Gierse et al., 2010; Castagna et al., 2016). In contrast, GLPG1690 lacks an acidic functional group and the X-ray structure of an analog was recently presented at the 2016 American Chemical Society National Meeting. This analog was shown to occupy both the competitive site and the non-competitive site, but lacked interaction with the Zn^{+2} atoms. Interestingly, although PAT-505 contains a carboxylic acid group, its binding is distinct from these ATX inhibitors. The X-ray structure for PAT-505 bound to human ATX shows that it binds in an allosteric site entirely away from the hydrophobic pocket and catalytic site, but maintains potent inhibition. This is consistent with that of the structurally similar non-competitive ATX inhibitor, PAT-347, which was also crystallized with human ATX and was found to bind exclusively in the hydrophobic channel (Stein et al., 2015). Interestingly, PAT-505 partially overlaps with GLPG1690 in the ATX hydrophobic channel. To date, although many ATX inhibitors have been published, very few have been evaluated in animal models of fibrosis and only one, GLPG1690, has entered clinical development. The identification of PAT-505, a potent and selective ATX inhibitor with good PK/PD properties, a novel binding mode and robust efficacy in a mouse NASH model paves the way for the design of additional inhibitors with physicochemical properties amenable to *in vivo* evaluation and clinical development.

Acknowledgements

We thank Deidre MacKenna for critical reading of the manuscript and the PharmAkea team for their contributions to the development of ATX inhibitors.

Authorship Contributions:

Participated in research design: Bain, Shannon, King, Hutchinson and Evans

Conducted experiments: Bain, Shannon, Darlington, Goulet, Prodanovich, Ma, Santini, Stein

Contributed new reagents or analytical tools: Huang, Lonergan, Calderon, Lai, Stein

Performed data analysis: Bain, Shannon, Darlington, Goulet, Prodanovich, Ma, Santini, Stein

Wrote or contributed to the writing of the manuscript: Bain, Shannon, Hutchinson and Evans

References

Aikawa S, Hashimoto T, Kano K and Aoki J (2015) Lysophosphatidic acid as a lipid mediator with multiple biological actions. *J Biochem* **157**:81-89.

Albers HM and Ovaa H (2012) Chemical evolution of autotaxin inhibitors. *Chem Rev* **112**:2593-2603.

Bai Z, Cai L, Umemoto E, Takeda A, Tohya K, Komai Y, Veeraveedu PT, Hata E, Sugiura Y, Kubo A, Suematsu M, Hayasaka H, Okudaira S, Aoki J, Tanaka T, Albers HM, Ovaa H and Miyasaka M (2013) Constitutive lymphocyte transmigration across the basal lamina of high endothelial venules is regulated by the autotaxin/lysophosphatidic acid axis. *J Immunol* **190**:2036-2048.

Black KE, Berdyshev E, Bain G, Castelino FV, Shea BS, Probst CK, Fontaine BA, Bronova I, Goulet L, Lagares D, Ahluwalia N, Knipe RS, Natarajan V and Tager AM (2016) Autotaxin activity increases locally following lung injury, but is not required for pulmonary lysophosphatidic acid production or fibrosis. *FASEB J* **30**:2435-2450.

Castagna D, Budd DC, Macdonald SJ, Jamieson C and Watson AJ (2016) Development of Autotaxin Inhibitors: An Overview of the Patent and Primary Literature. *J Med Chem*.

Castelino FV, Seiders J, Bain G, Brooks SF, King CD, Swaney JS, Lorrain DS, Chun J, Luster AD and Tager AM (2011) Amelioration of dermal fibrosis by genetic deletion or pharmacologic antagonism of lysophosphatidic acid receptor 1 in a mouse model of scleroderma. *Arthritis Rheum* **63**:1405-1415.

Cave MC, Clair HB, Hardesty JE, Falkner KC, Feng W, Clark BJ, Sidey J, Shi H, Aqel BA, McClain CJ and Prough RA (2016) Nuclear receptors and nonalcoholic fatty liver disease. *Biochim Biophys Acta*.

Folch J, Lees M and Sloane Stanley GH (1957) A simple method for the isolation and purification of total lipides from animal tissues. *J Biol Chem* **226**:497-509.

Geng H, Lan R, Singha PK, Gilchrist A, Weinreb PH, Violette SM, Weinberg JM, Saikumar P and Venkatachalam MA (2012) Lysophosphatidic acid increases proximal tubule cell secretion of

profibrotic cytokines PDGF-B and CTGF through LPA2- and Galphaq-mediated Rho and alphavbeta6 integrin-dependent activation of TGF-beta. *Am J Pathol* **181**:1236-1249.

Gierse J, Thorarensen A, Beltey K, Bradshaw-Pierce E, Cortes-Burgos L, Hall T, Johnston A, Murphy M, Nemirovskiy O, Ogawa S, Pegg L, Pelc M, Prinsen M, Schnute M, Wendling J, Wene S, Weinberg R, Wittwer A, Zweifel B and Masferrer J (2010) A novel autotaxin inhibitor reduces lysophosphatidic acid levels in plasma and the site of inflammation. *J Pharmacol Exp Ther* **334**:310-317.

Hausmann J, Kamtekar S, Christodoulou E, Day JE, Wu T, Fulkerson Z, Albers HM, van Meeteren LA, Houben AJ, van Zeijl L, Jansen S, Andries M, Hall T, Pegg LE, Benson TE, Kasiem M, Harlos K, Kooi CW, Smyth SS, Ovaa H, Bollen M, Morris AJ, Moolenaar WH and Perrakis A (2011) Structural basis of substrate discrimination and integrin binding by autotaxin. *Nat Struct Mol Biol* **18**:198-204.

Huang LS, Fu P, Patel P, Harijith A, Sun T, Zhao Y, Garcia JG, Chun J and Natarajan V (2013) Lysophosphatidic acid receptor-2 deficiency confers protection against bleomycin-induced lung injury and fibrosis in mice. *Am J Respir Cell Mol Biol* **49**:912-922.

Ikeda H, Yatomi Y, Yanase M, Satoh H, Nishihara A, Kawabata M and Fujiwara K (1998) Effects of lysophosphatidic acid on proliferation of stellate cells and hepatocytes in culture. *Biochem Biophys Res Commun* **248**:436-440.

Jansen S, Andries M, Vekemans K, Vanbilloen H, Verbruggen A and Bollen M (2009) Rapid clearance of the circulating metastatic factor autotaxin by the scavenger receptors of liver sinusoidal endothelial cells. *Cancer Lett* **284**:216-221.

Kleiner DE, Brunt EM, Van Natta M, Behling C, Contos MJ, Cummings OW, Ferrell LD, Liu YC, Torbenson MS, Unalp-Arida A, Yeh M, McCullough AJ, Sanyal AJ and Nonalcoholic Steatohepatitis Clinical Research N (2005) Design and validation of a histological scoring system for nonalcoholic fatty liver disease. *Hepatology* **41**:1313-1321.

Kondo M, Ishizawa T, Enooku K, Tokuhara Y, Ohkawa R, Uranbileg B, Nakagawa H, Tateishi R, Yoshida H, Kokudo N, Koike K, Yatomi Y and Ikeda H (2014) Increased serum autotaxin levels in hepatocellular carcinoma patients were caused by background liver fibrosis but not by carcinoma. *Clin Chim Acta* **433**:128-134.

Levesque SA, Lavoie EG, Lecka J, Bigonnesse F and Sevigny J (2007) Specificity of the ecto-ATPase inhibitor ARL 67156 on human and mouse ectonucleotidases. *Br J Pharmacol* **152**:141-150.

Matsumoto M, Hada N, Sakamaki Y, Uno A, Shiga T, Tanaka C, Ito T, Katsume A and Sudoh M (2013) An improved mouse model that rapidly develops fibrosis in non-alcoholic steatohepatitis. *Int J Exp Pathol* **94**:93-103.

McIntyre TM, Pontsler AV, Silva AR, St Hilaire A, Xu Y, Hinshaw JC, Zimmerman GA, Hama K, Aoki J, Arai H and Prestwich GD (2003) Identification of an intracellular receptor for lysophosphatidic acid (LPA): LPA is a transcellular PPARgamma agonist. *Proc Natl Acad Sci U S A* **100**:131-136.

Nakagawa H, Ikeda H, Nakamura K, Ohkawa R, Masuzaki R, Tateishi R, Yoshida H, Watanabe N, Tejima K, Kume Y, Iwai T, Suzuki A, Tomiya T, Inoue Y, Nishikawa T, Ohtomo N, Tanoue Y, Omata M, Igarashi K, Aoki J, Koike K and Yatomi Y (2011) Autotaxin as a novel serum marker of liver fibrosis. *Clin Chim Acta* **412**:1201-1206.

Nakamura K, Ohkawa R, Okubo S, Tozuka M, Okada M, Aoki S, Aoki J, Arai H, Ikeda H and Yatomi Y (2007) Measurement of lysophospholipase D/autotaxin activity in human serum samples. *Clin Biochem* **40**:274-277.

Nishimasu H, Okudaira S, Hama K, Mihara E, Dohmae N, Inoue A, Ishitani R, Takagi J, Aoki J and Nureki O (2011) Crystal structure of autotaxin and insight into GPCR activation by lipid mediators. *Nat Struct Mol Biol* **18**:205-212.

Oikonomou N, Mouratis MA, Tzouvelekis A, Kaffe E, Valavanis C, Vilaras G, Karameris A, Prestwich GD, Bouros D and Aidinis V (2012) Pulmonary autotaxin expression contributes to the pathogenesis of pulmonary fibrosis. *Am J Respir Cell Mol Biol* **47**:566-574.

Pleli T, Martin D, Kronenberger B, Brunner F, Koberle V, Grammatikos G, Farnik H, Martinez Y, Finkelmeier F, Labocha S, Ferreiros N, Zeuzem S, Piiper A and Waidmann O (2014) Serum autotaxin is a parameter for the severity of liver cirrhosis and overall survival in patients with liver cirrhosis--a prospective cohort study. *PLoS One* **9**:e103532.

Pradere JP, Gonzalez J, Klein J, Valet P, Gres S, Salant D, Bascands JL, Saulnier-Blache JS and Schanstra JP (2008) Lysophosphatidic acid and renal fibrosis. *Biochim Biophys Acta* **1781**:582-587.

Pradere JP, Tarnus E, Gres S, Valet P and Saulnier-Blache JS (2007) Secretion and lysophospholipase D activity of autotaxin by adipocytes are controlled by N-glycosylation and signal peptidase. *Biochim Biophys Acta* **1771**:93-102.

Rancoule C, Dusaulcy R, Treguer K, Gres S, Attane C and Saulnier-Blache JS (2014) Involvement of autotaxin/lysophosphatidic acid signaling in obesity and impaired glucose homeostasis. *Biochimie* **96**:140-143.

Rancoule C, Dusaulcy R, Treguer K, Gres S, Guigne C, Quilliot D, Valet P and Saulnier-Blache JS (2012) Depot-specific regulation of autotaxin with obesity in human adipose tissue. *J Physiol Biochem* **68**:635-644.

Ratziu V (2016) Novel Pharmacotherapy Options for NASH. *Dig Dis Sci* **61**:1398-1405.

Reeves VL, Trybula JS, Wills RC, Goodpaster BH, Dube JJ, Kienesberger PC and Kershaw EE (2015) Serum Autotaxin/ENPP2 correlates with insulin resistance in older humans with obesity. *Obesity (Silver Spring)* **23**:2371-2376.

Sakagami H, Aoki J, Natori Y, Nishikawa K, Kakehi Y, Natori Y and Arai H (2005) Biochemical and molecular characterization of a novel choline-specific glycerophosphodiester phosphodiesterase belonging to the nucleotide pyrophosphatase/phosphodiesterase family. *J Biol Chem* **280**:23084-23093.

Sakai N, Chun J, Duffield JS, Wada T, Luster AD and Tager AM (2013) LPA1-induced cytoskeleton reorganization drives fibrosis through CTGF-dependent fibroblast proliferation. *FASEB J* **27**:1830-1846.

Sevastou I, Kaffe E, Mouratis MA and Aidinis V (2013) Lysoglycerophospholipids in chronic inflammatory disorders: the PLA(2)/LPC and ATX/LPA axes. *Biochim Biophys Acta* **1831**:42-60.

Stein AJ, Bain G, Prodanovich P, Santini AM, Darlington J, Stelzer NM, Sidhu RS, Schaub J, Goulet L, Lonergan D, Calderon I, Evans JF and Hutchinson JH (2015) Structural Basis for Inhibition of Human Autotaxin by Four Potent Compounds with Distinct Modes of Binding. *Mol Pharmacol* **88**:982-992.

Stracke ML, Krutzsch HC, Unsworth EJ, Arestad A, Cioce V, Schiffmann E and Liotta LA (1992) Identification, purification, and partial sequence analysis of autotaxin, a novel motility-stimulating protein. *J Biol Chem* **267**:2524-2529.

Sun H, Huang FF and Qu S (2015) Melatonin: a potential intervention for hepatic steatosis. *Lipids Health Dis* **14**:75.

Swaney JS, Chapman C, Correa LD, Stebbins KJ, Broadhead AR, Bain G, Santini AM, Darlington J, King CD, Baccei CS, Lee C, Parr TA, Roppe JR, Seiders TJ, Ziff J, Prasit P, Hutchinson JH, Evans JF and Lorrain DS (2011) Pharmacokinetic and pharmacodynamic characterization of an oral lysophosphatidic acid type 1 receptor-selective antagonist. *J Pharmacol Exp Ther* **336**:693-700.

Swaney JS, Chapman C, Correa LD, Stebbins KJ, Bundey RA, Prodanovich PC, Fagan P, Baccei CS, Santini AM, Hutchinson JH, Seiders TJ, Parr TA, Prasit P, Evans JF and Lorrain DS (2010) A novel, orally active LPA(1) receptor antagonist inhibits lung fibrosis in the mouse bleomycin model. *Br J Pharmacol* **160**:1699-1713.

Tager AM, LaCamera P, Shea BS, Campanella GS, Selman M, Zhao Z, Polosukhin V, Wain J, Karimi-Shah BA, Kim ND, Hart WK, Pardo A, Blackwell TS, Xu Y, Chun J and Luster AD (2008) The

lysophosphatidic acid receptor LPA1 links pulmonary fibrosis to lung injury by mediating fibroblast recruitment and vascular leak. *Nat Med* **14**:45-54.

Tanaka M, Okudaira S, Kishi Y, Ohkawa R, Iseki S, Ota M, Noji S, Yatomi Y, Aoki J and Arai H (2006) Autotaxin stabilizes blood vessels and is required for embryonic vasculature by producing lysophosphatidic acid. *J Biol Chem* **281**:25822-25830.

Umezu-Goto M, Kishi Y, Taira A, Hama K, Dohmae N, Takio K, Yamori T, Mills GB, Inoue K, Aoki J and Arai H (2002) Autotaxin has lysophospholipase D activity leading to tumor cell growth and motility by lysophosphatidic acid production. *J Cell Biol* **158**:227-233.

van Meeteren LA, Ruurs P, Stortelers C, Bouwman P, van Rooijen MA, Pradere JP, Pettit TR, Wakelam MJ, Saulnier-Blache JS, Mummery CL, Moolenaar WH and Jonkers J (2006) Autotaxin, a secreted lysophospholipase D, is essential for blood vessel formation during development. *Mol Cell Biol* **26**:5015-5022.

Watanabe N, Ikeda H, Nakamura K, Ohkawa R, Kume Y, Aoki J, Hama K, Okudaira S, Tanaka M, Tomiya T, Yanase M, Tejima K, Nishikawa T, Arai M, Arai H, Omata M, Fujiwara K and Yatomi Y (2007a) Both plasma lysophosphatidic acid and serum autotaxin levels are increased in chronic hepatitis C. *J Clin Gastroenterol* **41**:616-623.

Watanabe N, Ikeda H, Nakamura K, Ohkawa R, Kume Y, Tomiya T, Tejima K, Nishikawa T, Arai M, Yanase M, Aoki J, Arai H, Omata M, Fujiwara K and Yatomi Y (2007b) Plasma lysophosphatidic acid level and serum autotaxin activity are increased in liver injury in rats in relation to its severity. *Life Sci* **81**:1009-1015.

Yanase M, Ikeda H, Matsui A, Maekawa H, Noiri E, Tomiya T, Arai M, Yano T, Shibata M, Ikebe M, Fujiwara K, Rojkind M and Ogata I (2000) Lysophosphatidic acid enhances collagen gel contraction by hepatic stellate cells: association with rho-kinase. *Biochem Biophys Res Commun* **277**:72-78.

JPET Fast Forward. Published on October 17, 2016 as DOI: 10.1124/jpet.116.237156
This article has not been copyedited and formatted. The final version may differ from this version.

Figure Legends

Fig. 1. Chemical structures of PAT-505 (A), PF-8380 (B), GLPG1690 (C) and PAT-048 (D).

Fig. 2. Schematic diagrams for the study designs of the mouse acute CCl_4 PK/PD model (A), the mouse STAM™ NASH model (B) and the mouse CDAHFD NASH model (C). For the acute CCl_4 PK/PD model, male BALB/c (n=8/group) mice were administered CCl_4 intraperitoneally at time 0 h. PAT-505 was administered orally at either 8 h or 22 h after CCl_4 administration for determination of drug concentrations and ATX activity at approximately trough and peak drug concentrations, respectively. Blood and liver were collected at time 24 h. (B) For the mouse STAM™ model, animals (n= 6-8/group) were injected with streptozotocin two days after birth then fed a high-fat diet starting at 4 weeks after birth. PAT-505, vehicle or the positive control (Telmisartan) was dosed from week 6 to 12 and blood and liver collected at week 12. In the CDAHFD NASH model, animals (n=7-10/group) were CDAHFD fed for 12 weeks with dosing of PAT-505 (or vehicle) starting after 5 weeks of CDAHFD feeding. Blood and liver were collected at week 12.

Fig. 3. Effect of PAT-505 on *in vitro* and *ex vivo* ATX lysoPLD activity. Concentration response curves for the inhibition of ATX lysoPLD activity in the Hep3B TOOS assay (A), the human blood assay (B) and the mouse plasma assay (C). Data represents the mean ± SEM of at least 3 independent experiments. Substrate/velocity curves and alpha value (D) for ATX lysoPLD activity in the presence of varying concentrations (0.5X-4X the IC_{50} value) of PAT-505. (E) Plots of K_m and V_{max} values vs. inhibitor concentration. The K_m and V_{max} values were derived from the substrate/velocity curve shown in D.

Fig. 4. Pharmacokinetic and pharmacodynamic profile of PAT-505 in mouse and rat. PAT-505 plasma concentrations and plasma ATX lysoPLD activity were analyzed at various times (0.5-24 h) after a single oral administration of PAT-505 to (A) mice (30 mg/kg, n=3/group) or (B) rats (10 mg/kg, n=3). Plotted is the mean ± SEM. The dotted line represents the *in vitro* plasma IC_{90} value from the mouse and rat assays (~630 nM and ~770 nM, respectively).

Fig. 5. Effect of PAT-505 on *in vivo* inhibition of ATX lysoPLD activity in plasma and liver. Mice (n= 8/group) were injected intraperitoneally with CCl_4 and then administered a single oral dose of PAT-505 at either 2 h or 16 h prior to harvest. Blood and liver were collected 24 h post-CCl_4 and ATX lysoPLD activity evaluated in plasma and liver homogenates. Plotted are the individual values for each animal with the mean ± SEM indicated. Significance relative to Veh is noted with asterisks.

Fig. 6. Effect of PAT-505 treatment on hepatic steatosis, inflammation and fibrosis in the mouse STAM™ NASH model. Mice (n= 6-8/group) were injected subcutaneously with streptozotocin and then fed a high-fat diet. PAT-505 at 10 or 30 mg/kg BID or Telmisartan at 5 mg/kg was dosed daily from week 6-12 and blood and liver harvested at week 12. Histopathology of H&E stained liver sections was used to score hepatic inflammation (A), hepatocellular ballooning (B) and steatosis (C). NAS score (D) represents the composite of the steatosis, inflammation, and hepatocyte ballooning scores. (E) Quantitation of PSR positive area from PSR stained liver sections. Plotted are the individual values for each animal with the mean ± SEM indicated.

Fig. 7. Effect of PAT-505 treatment on hepatic steatosis, inflammation and fibrosis in the mouse CDAHFD NASH model. Mice (n=7-10/group) were fed a choline-deficient diet containing 0.1% methionine and high-fat for 12 weeks. PAT-505 at 30 mg/kg was administered orally once daily

from week 5-12 and blood and liver harvested at week 12. Representative PSR-stained liver sections (A) that were used to generate the fibrosis score data (C) and anti-α-SMA stained liver sections (B) that were used to generate the α-SMA score data (D). (E) Serum bilirubin concentrations and (F) total liver triglyceride concentrations. Plasma ATX activity (G) and plasma and liver PAT-505 concentrations (H) at 24 h post-last dose. Dotted line in (H) represents the IC_{90} concentration for inhibition in the *in vitro* mouse plasma assay. For C-G, plotted are the individual values for each animal with the mean ± SEM indicated. For H, plotted are the individual values for each animal with the mean ± SD indicated.

JPET Fast Forward. Published on October 17, 2016 as DOI: 10.1124/jpet.116.237156
This article has not been copyedited and formatted. The final version may differ from this version.

TABLE 1.

IC_{50} values for PAT-505 and three reference ATX inhibitors (PF-8380, GLPG1690 and PAT-048) in three different *in vitro* lysoPLD assays. All IC_{50} values shown are the geometric mean (nM) x/÷ geometric standard deviation with the *n* values indicated in parentheses.

	IC_{50} (nM)			
LysoPLD Assay	PAT-505	PF-8380	GLPG1690	PAT-048
Hep3B (TOOS)	2.0 x/÷ 1.18 (7)	7.1 x/÷ 1.19 (9)	180 x/÷ 1.13 (3)	1.1 x/÷ 1.38 (7)
Human Blood (20:4 LPA)	9.7 x/÷ 2.43 (6)	280 x/÷ 1.54 (9)	82 x/÷ 1.26 (3)	8.9 x/÷ 1.60 (5)
Mouse Plasma (20:4 LPA)	62 x/÷ 2.22 (7)	320 x/÷ 1.62 (5)	360 x/÷ 1.09 (3)	22 x/÷ 1.55 (4)

JPET Fast Forward. Published on October 17, 2016 as DOI: 10.1124/jpet.116.237156
This article has not been copyedited and formatted. The final version may differ from this version.

TABLE 2.

Pharmacokineic parameters for PAT-505 in mouse and rat after either intravenous (i.v.) or oral (p.o.) administration.

	Mouse i.v.	Mouse p.o.	Rat i.v.	Rat p.o.
Dose (mg/kg)	5	30	0.2	10
AUC (hr*µg/mL)	42.4	145.6	13.0	337.7
Dose-adjusted AUC	8.5	4.9	65	33.8
Cl_{Pl} (mL/min/kg)	2.0		0.22	
VDss (L/kg)	0.41		0.16	
$t_{1/2}$ (h)	3.9	3.3	10.2	6.9
%F		57		52
C0 (µg/mL)	59.1		4.1	
C_{max} (µg/mL)		22.7		33.9
T_{max} (h)		4.0		3.3

JPET Fast Forward. Published on October 17, 2016 as DOI: 10.1124/jpet.116.237156
This article has not been copyedited and formatted. The final version may differ from this version.

TABLE 3.

Serum liver enzymes and total liver triglycerides from CDAHFD study. All values represent the mean ± SEM.

Treatment	ALT (U/L)	AST (U/L)	ALP (U/L)	Total BR (mg/dL)	Liver Tg (nmol/mg)
Normal chow/Veh	25 ± 1	141 ± 16	54 ± 3	0.17 ± 0.02	19 ± 1
CDAHFD/Veh	260 ± 19	290 ± 14	106 ± 3	0.41 ± 0.04	200 ± 3
CDAHFD/PAT-505	217 ± 19	225 ± 13*	106 ± 4	0.20 ± 0.02***	182 ± 3 ***

*p=0.01; ***p<0.001

JPET Fast Forward. Published on October 17, 2016 as DOI: 10.1124/jpet.116.237156
This article has not been copyedited and formatted. The final version may differ from this version.

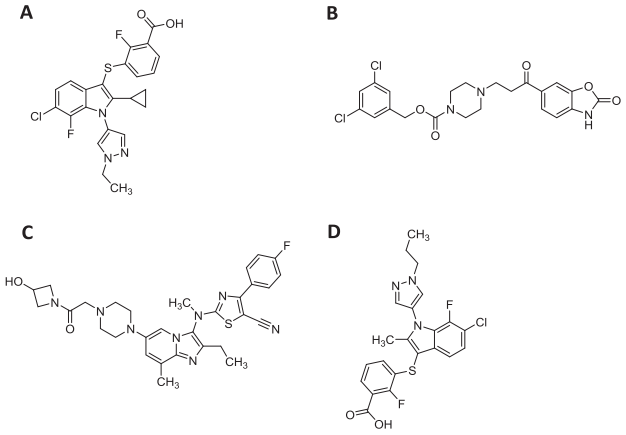

Figure 1

JPET Fast Forward. Published on October 17, 2016 as DOI: 10.1124/jpet.116.237156
This article has not been copyedited and formatted. The final version may differ from this version.

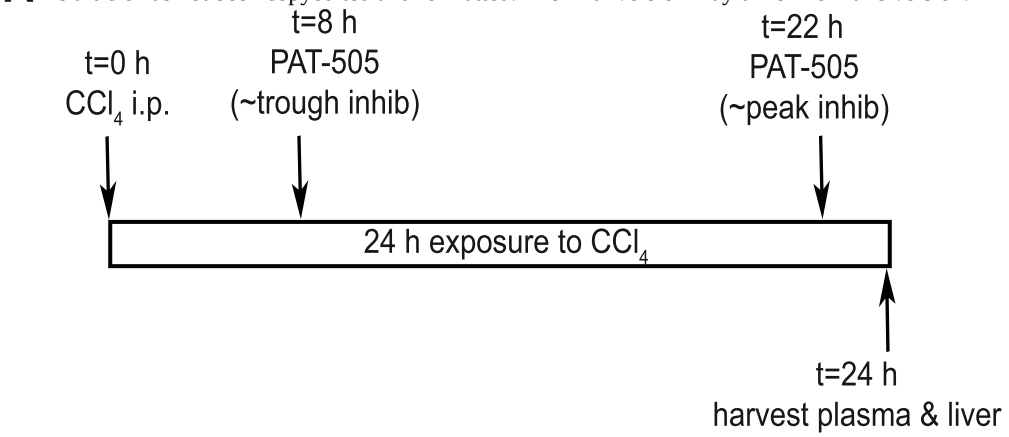

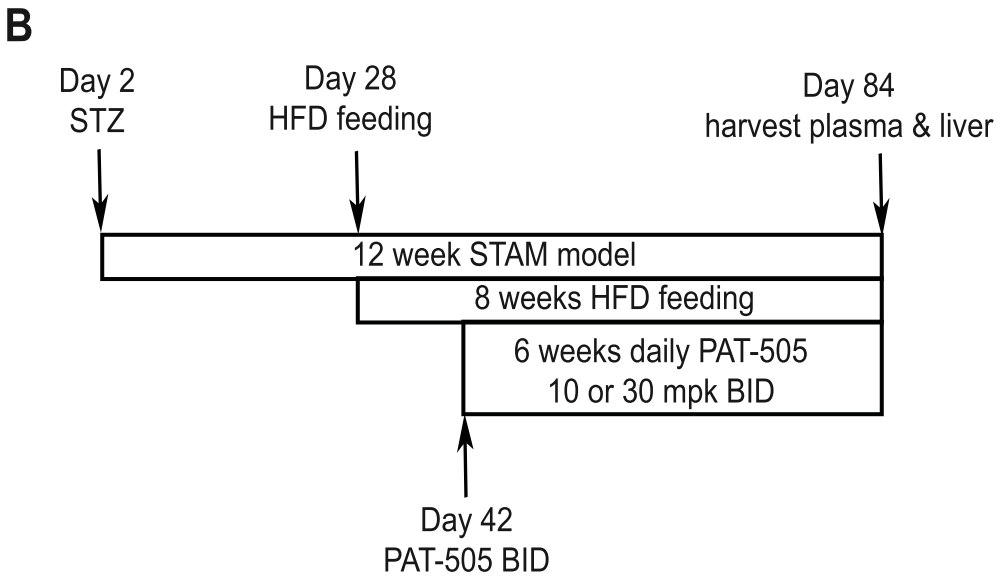

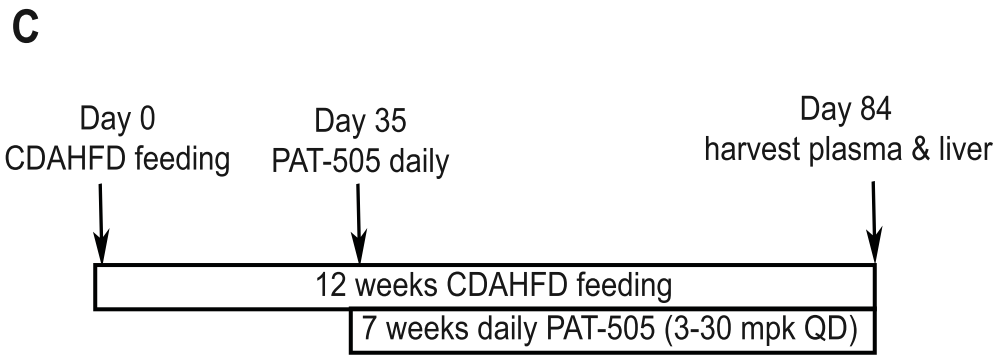

Figure 2

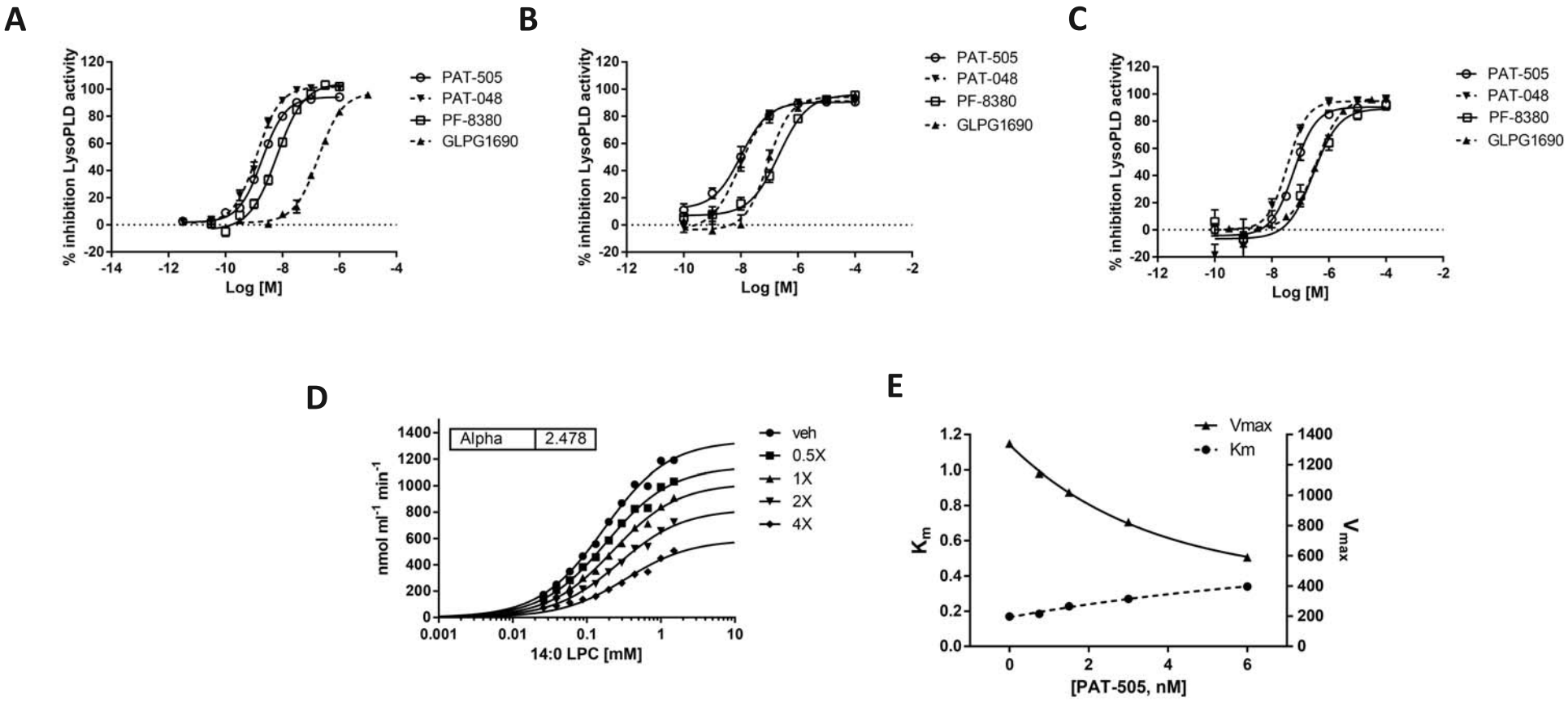

Figure 3

JPET Fast Forward. Published on October 17, 2016 as DOI: 10.1124/jpet.116.237156
This article has not been copyedited and formatted. The final version may differ from this version.

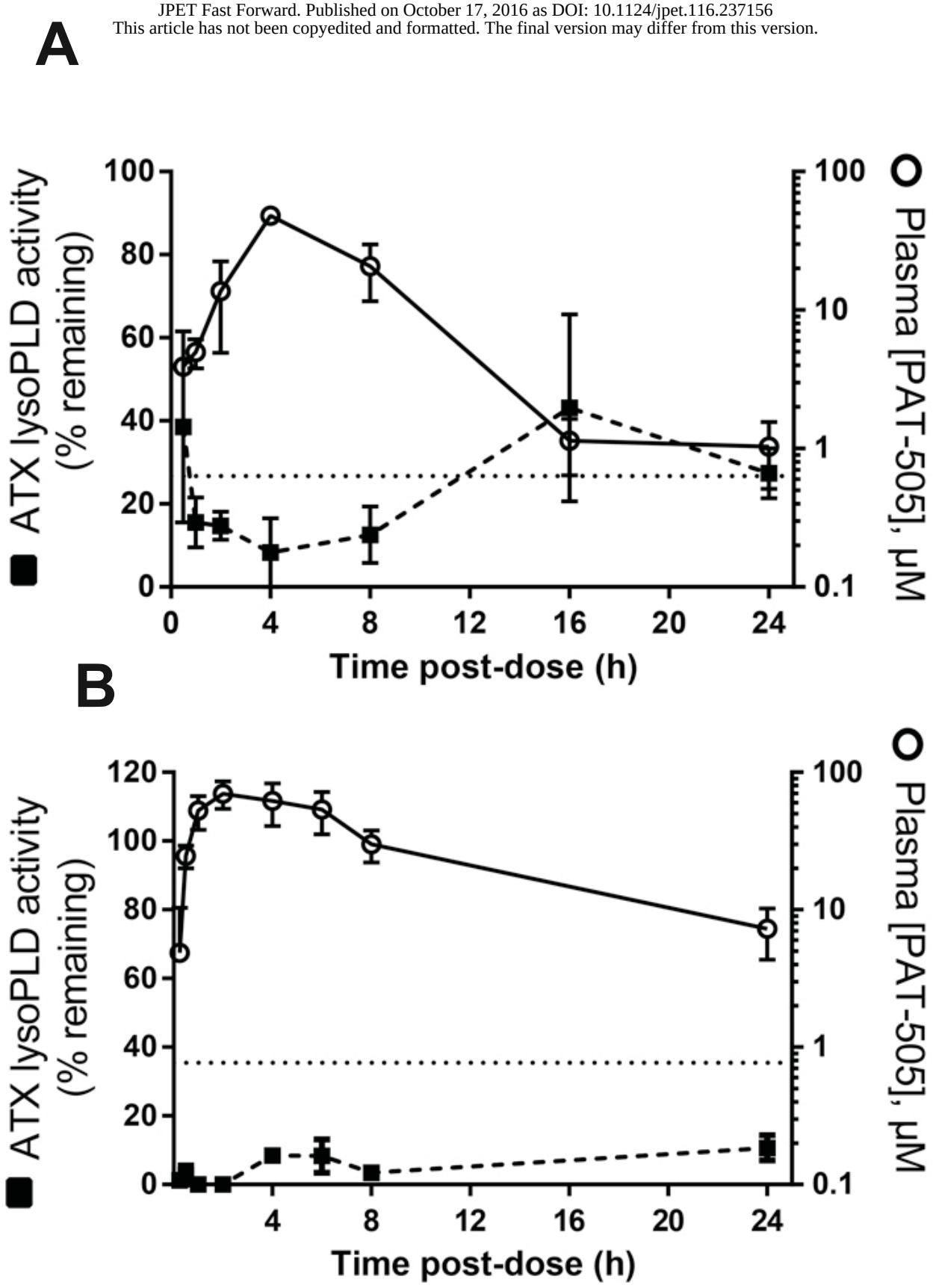

Figure 4

JPET Fast Forward. Published on October 17, 2016 as DOI: 10.1124/jpet.116.237156
This article has not been copyedited and formatted. The final version may differ from this version.

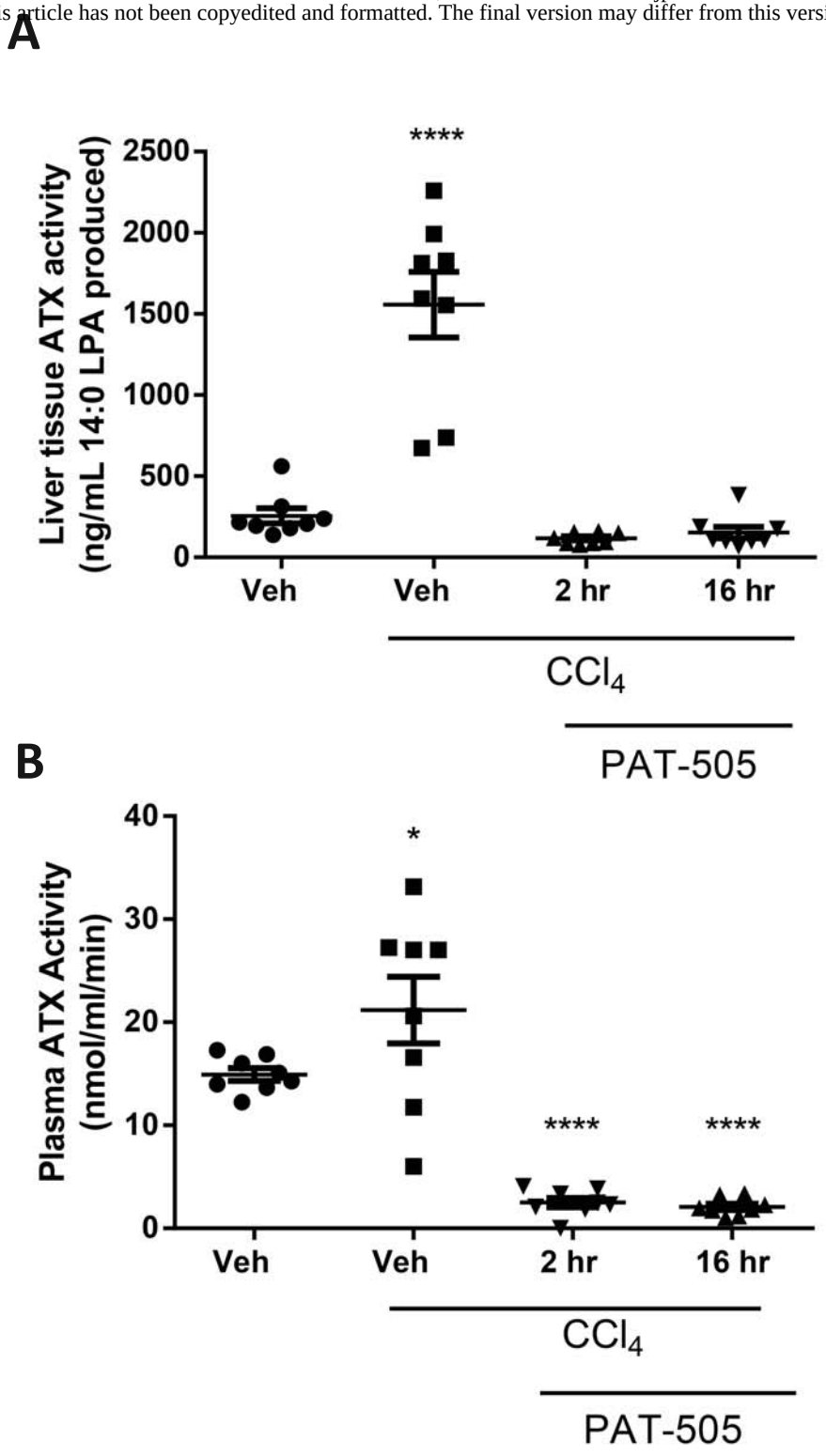

Figure 5

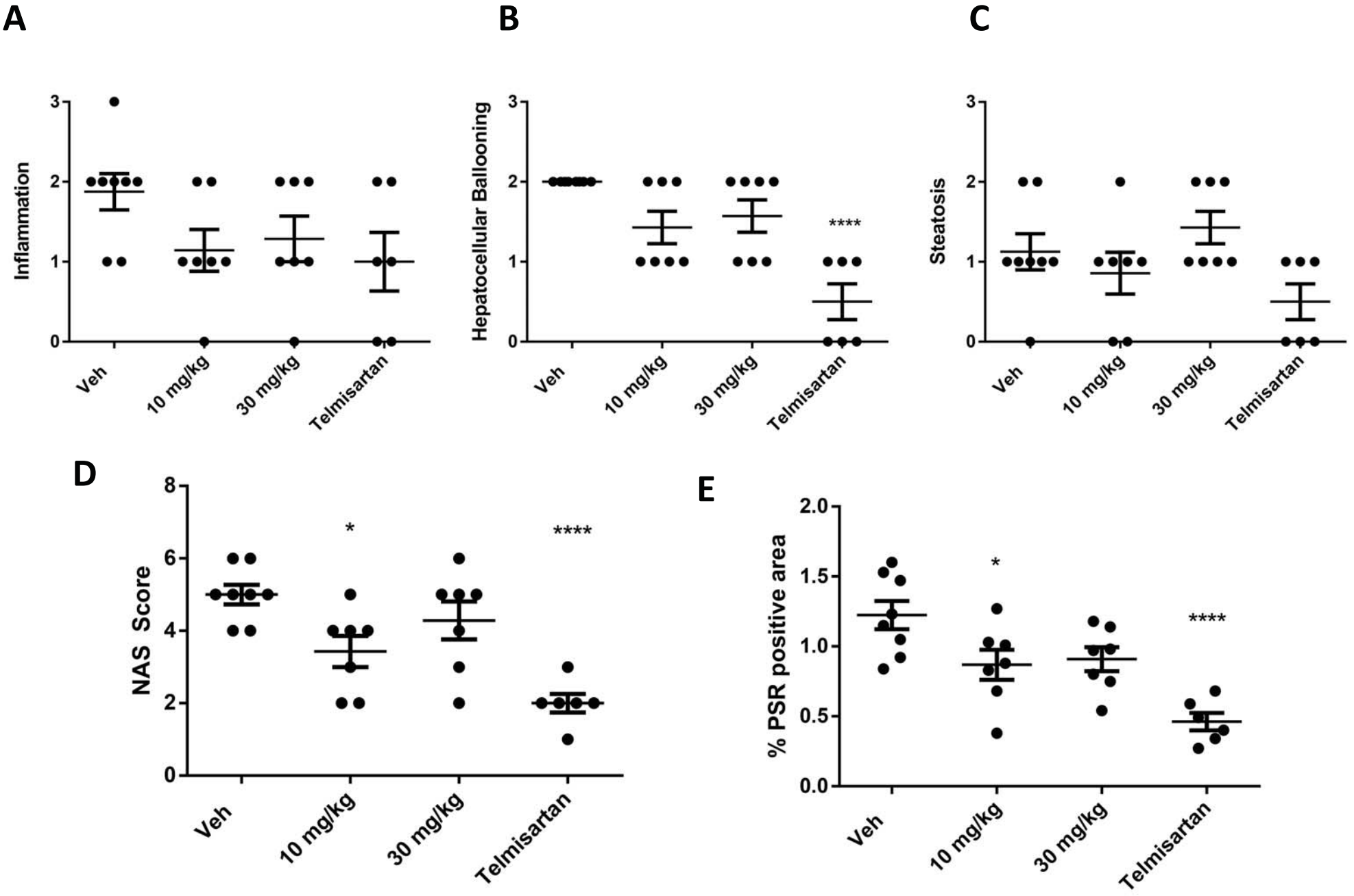

Figure 6

JPET Fast Forward. Published on October 17, 2016 as DOI: 10.1124/jpet.116.237156
This article has not been copyedited and formatted. The final version may differ from this version.

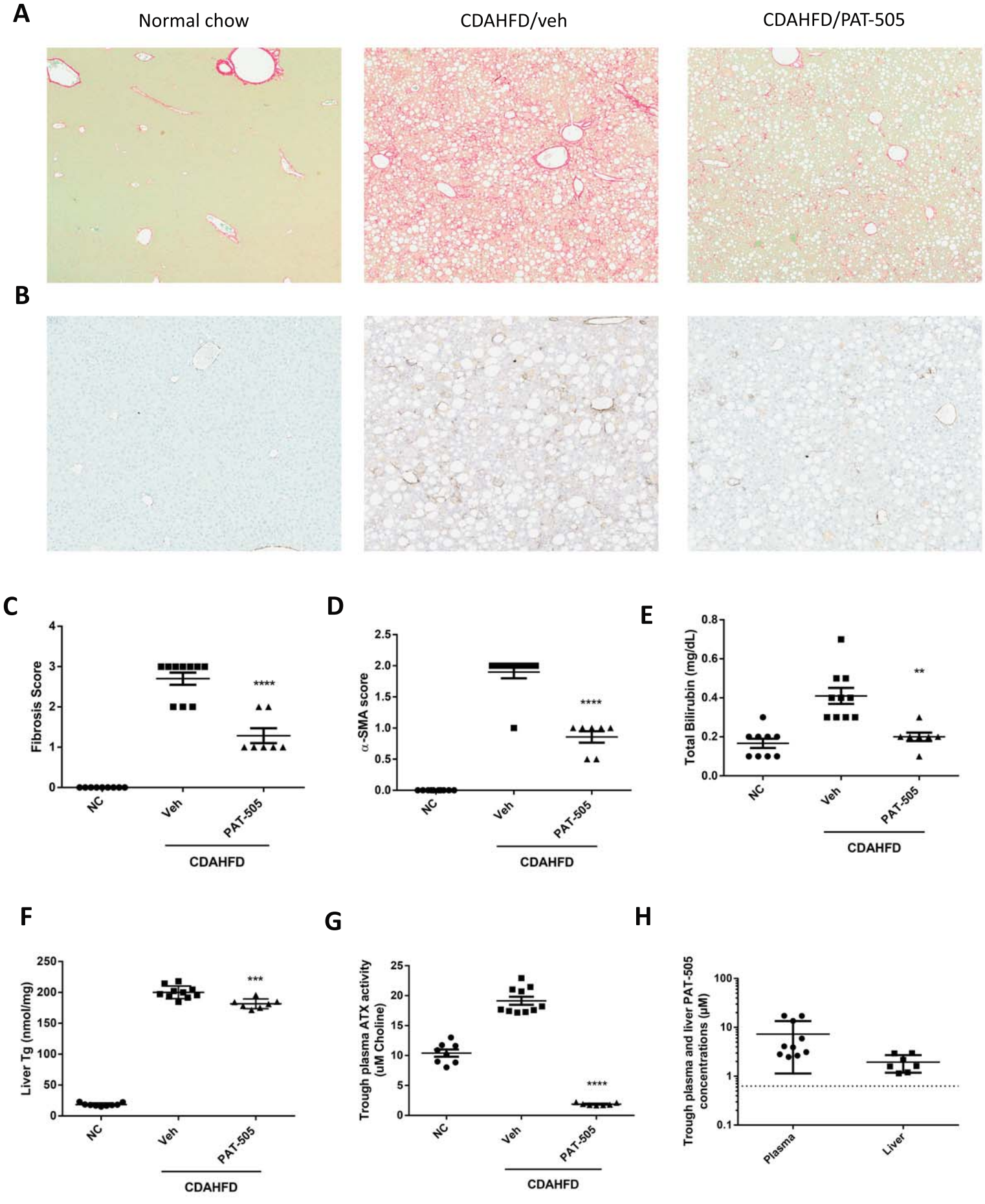

Figure 7